Clean Energy, 2021, 354–374

doi: 10.1093/ce/zkab016
Homepage: https://academic.oup.com/ce

RESEARCH ARTICLE

Flexible sodium-ion batteries using electrodes from *Samanea saman* tree leaf-derived carbon quantum dots decorated with SnO_2 and $NaVO_3$

Baskar Thangaraj[1], Surawut Chuangchote[2,3], Nutthapon Wongyao[4], Pravin Raj Solomon[5], Kamonchanok Roongraung[3,6], Wachira Chaiworn[1] and Werasak Surareungchai[7,*]

[1]Pilot Plant Development and Training Institute, King Mongkut's University of Technology Thonburi, Bangkhuntien-chaitalay Road, Thakam, Bangkok-10150, Thailand
[2]Department of Tool and Materials Engineering, Faculty of Engineering, King Mongkut's University of Technology Thonburi, 126 Prachauthit Road, Bangmod, Thungkru, Bangkok 10140, Thailand
[3]Research Center of Advanced Materials for Energy and Environmental Technology, King Mongkut's University of Technology Thonburi, 126 Prachauthit Road, Bangmod, Bangkok 10140, Thailand
[4]Fuel Cells and Hydrogen Research and Engineering Center, Pilot Plant Development and Training Institute, King Mongkut's University of Technology Thonburi, Bangkok 10140, Thailand
[5]School of Chemical and Biotechnology, SASTRA-Deemed University, Thanjavur-613 402, Tamil Nadu, India
[6]Integrative Biorefinery Laboratory, National Center for Genetic Engineering and Biotechnology, National Science and Technology Development Agency, Patumthani-12120, Thailand
[7]School of Bioresources Technology, and Nanoscience & Nanotechnology Graduate Programme, Faculty of Science, King Mongkut's University of Technology Thonburi, Bangkhuntien-chaitalay Road, Thakam, Bangkok 10150, Thailand

*Corresponding author. E-mail: werasak.sur@kmutt.ac.th

Abstract

Carbonaceous materials with large interlayer spacing and disordered structure are considered suitable as electrodes in sodium-ion batteries so as to overcome the problem encountered in conventional electrodes. In this study, carbon quantum dots (CQDs) decorated with SnO_2 and $NaVO_3$ are used as electrodes in the fabrication of flexible Na-ion batteries. CQDs are prepared from dead leaves of the *Samanea saman* tree through alkaline-peroxide treatment and hydrothermal carbonization. As-prepared CQDs exhibit a quantum yield of 21.03% at an excitation wavelength of 360 nm. Various separators such as indium-doped tin oxide/polyoxyethylene tridecyl ether (ITO/PTE), rice paper (RP), silicone with three big holes (SIL BH), silicone with many small holes (SIL SH) and cellulose paper (CP) have been tried in flexible Na-ion batteries. SIL SH achieved higher specific capacitance (881 F g^{-1}) than other separators due to the function of many small holes on the surface of the silicone. The SIL SH separator delivered higher discharge capacities of 141 and 114 mC g^{-1} at 1.5 and 2.5 V than SIL BH. The RP separator delivered specific discharge capacities of 1087 and 347 mC g^{-1} in the 1st and 50th cycles, respectively,

Received: 9 February 2021; **Accepted:** 3 May 2021

at 1 V. The RP separator delivered a high initial specific discharge capacity of 698 mC g^{-1} at 2 V and maintained a good discharge capacity of 222 mC g^{-1} in the 50th cycle. As compared to RP, SIL SH delivered high specific discharge capacity of 4246 in 1st cycle at 2 V but maintained a capacity of 71 mC g^{-1} in the 50th cycle. This study reveals the scope of developing flexible Na-ion batteries with high capacity and cyclability using carbonaceous materials derived from the leaves of the *S. saman* tree.

Graphical Abstract

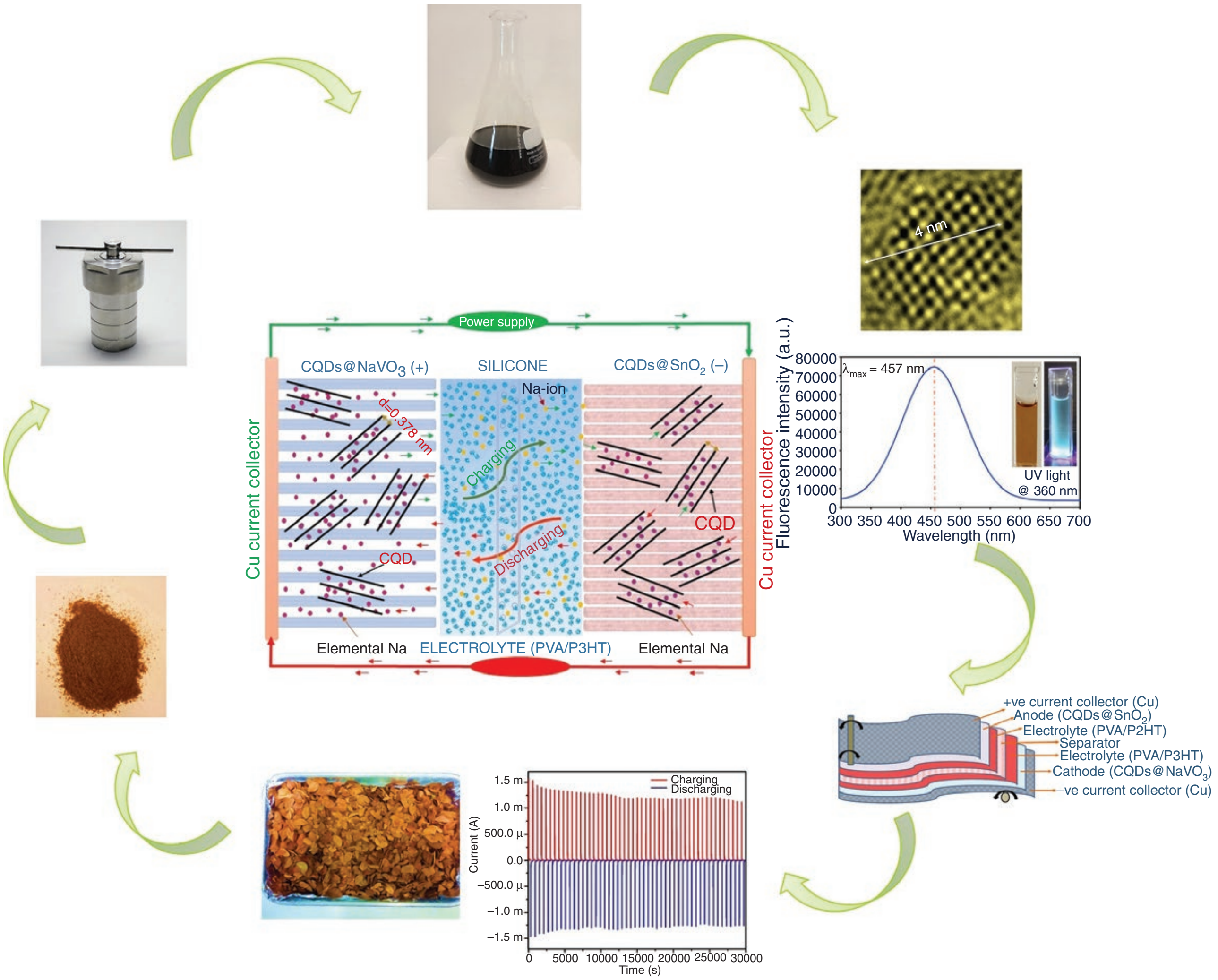

Keywords: biomass; carbon quantum dots; separators; gel-polymer electrolyte; flexible Na-ion battery

Introduction

Energy-storage technology has become a growing global concern over the past decade due to the practical application of renewable energy resources and environmental exigencies [1]. Alternate energy sources such as wind and photovoltaic technology are poised to complement the energy demand and are becoming increasingly prominent in several industrialized countries. The electricity thus produced is transferred into energy-storage devices of load-levelling transformers. Then, it is distributed to consumers through electrical grids [2]. Portable energy-storage devices may have their use in hybrid electric vehicles, plug-in hybrid electric vehicles and in sole electric vehicles (EVs). In addition, it plays an important role as an electronic component in supercapacitors, fuel cells and batteries. Among the many commercial storage provisions available on the market, Li-ion batteries (LIBs) have expanded their roles in EVs and power stations [3–5].

The LIB has immense electrochemical properties such as high voltage, high energy density and high specific power as well as a wide range of operating temperatures with good durability. As Li is a lightweight metallic element, it has a low redox potential ($E^{0}_{(Li^{+}/Li)}$ = –3.04 V versus a standard hydrogen electrode (SHE)). In addition, it easily diffuses in solids due to its low radius (0.76 Å) [3]. Currently, LIBs have penetrated the portable electronic market and have become the candidate to power the next generation of EVs. However, the development of rechargeable LIBs is still facing a series of challenges due to the limitation posed on cathode materials. In addition, lithium has low terrestrial reserves and is being sourced in geopolitically sensitive areas. The cost of lithium is prone to increase as the demand increases due to the large-scale development of EVs and hybrid EVs. Another concern is that the disposing of spent batteries may create soil pollution [6]. It is felt that the use of Na instead of Li in rocking-chair batteries can alleviate the problem posed by lithium. Sodium has the advantage of being the sixth most abundant element in Earth's crust (23 600 ppm on average), is easy to recover and is low-cost with a suitable redox potential of –2.71 V [7–9]. Even so, one of the major critical issues in the development of high-performance sodium-ion batteries (SIBs) is the lack of ideal conducting materials for use in electrodes. Nanostructured carbon materials, especially carbon quantum dots (CQDs), have been considered as one of the most promising electrodes for SIBs, due to their ideal electrical conductivity, chemical stability, compatibility, abundance, low cost and sustainability [10]. In addition, nanostructured carbon materials with micro or mesopores create channels for ion diffusion so as to accelerate the electrochemical reactions [11]. These pores offer suitable channels for the permeation of anions and cations that also endure the volume expansion of the graphite layer in the nanostructured carbon materials [1].

The light-emitting quantum-sized carbon dots are <10 nm in size and are known to be favourable as alternate semiconducting materials to Si and Ge in various applications due to their extra small size, hydrophilicity and biocompatibility with excellent photoluminescence [12]. Generally, CQDs are synthesized from chemical precursors. Recently, biomass wastes are being used as potential alternative feedstock for CQDs due to economic and environmental considerations [13, 14]. Recently, many works have reported on the synthesis of CQDs from waste biomass such as the peels of oranges [15], watermelon [16] and chestnut (*Trapabispinosa*) [17], and certain plant leaves [18]. Biomass-based CQDs tend to avoid the growing consumption of recalcitrant chemicals. In addition, biomass-derived carbon electrodes have many advantages such as a high specific surface area, large interlayer spacing, well defined distribution of pore size, excellent electric conductivity and surface chemistry amenable for easy modification [19]. Quantum-sized CQDs enhance reaction kinetics, accommodate volume changes of active materials and reduce the ionic diffusion path [20].

Several transition-metal oxides have been widely used as anodes including SnO_2 [21], FeO [22], CoO [23], NiO, Co_3O_4, Mn_3O_4 and Fe_3O_4 [24]. Among them, SnO_2 has been preferred as a promising anode material due to its relatively high theoretical specific capacitance (~782 mAh g^{-1}), which is higher than that of commercial graphite (~370 mAh g^{-1}). Besides, it is of low cost and is formed of a hierarchical hollow structure. Pure SnO_2 is inhibited by its large initial capacity loss and severe capacity fading, volume changes due to the agglomeration of tin nanoparticles during alloying and de-alloying processes with metal ions affecting the pulverization and loss of electrical contact in the electrodes. In this context, it is found to be better to design an SnO_2 composite typically combined with carbonaceous materials especially CQDs to enhance the intrinsic properties. For instance, carbon-coated hierarchical SnO_2 hollow spheres are reported to deliver as high as 1307.4 mAh g^{-1} at 100 mA g^{-1} [21].

Many cathode materials including layered transition-metal oxides, transition-metal fluorides, phosphates, fluorophosphates, pyrophosphates, sulphides, sulphates, Prussian blue and organic polymers have been explored for use in SIBs. Among these, vanadium(V)-based cathode materials, especially sodium-layered oxides (Na_xVO_2), have been considered as efficient electrodes due to their high operating voltages, theoretical capacities and energy densities as well as their rich electrochemical reaction [25]. NaV_6O_{15} shows high performance in LIBs whereas its cyclability and rate capability are poor in SIBs. Therefore, carbon is coated on the surface of the electrode to increase the electrical conductivity and facilitate electron transportation in the electrode as well as to improve the cyclability during long-term charge and discharge processes [26]. Song *et al.* reported that the hierarchical architecture of carbon-coated NaV_6O_{15} nanotubes delivered an initial capacity of 168 mA g^{-1} and reached a maximum capacity rate of 209 mAh g^{-1} at 0.1°C [27].

Gel-polymer electrolytes (GPEs) play an important role in flexible batteries. GPEs overcome the issues of liquid electrolytes especially in flexible batteries by replacing liquid electrolytes so as to prevent any leakage. GPEs with an inherent flexibility offer a wide potential electrochemical window with low toxicity and high safety. GPEs have been widely used in flexible batteries due to their good ionic conductivity, non-flammability, high thermal stability, resistance to leakage and mechanical stability [28]. Poly(acrylonitrile) (PAN)-based gel electrolytes have high ionic conductivity (~10^{-3} S cm^{-1}) at 25°C [29]. For instance, high-performance GPEs comprising polyacrylonitrile/thermoplastic polyurethane/polystyrene (PAN/TPU/PS) exhibit a maximum ionic conductivity of 3.9×10^{-3} S cm^{-1} at room temperature with an electrochemical stability of 5.8 V [30]. In addition to the above, the role of separators needs to be studied, as they are an integral part of the battery.

In the present study, CQDs are synthesized from dead leaves of the tree *Samanea saman* by an alkaline-peroxide-assisted hydrothermal carbonization (HTC) method. Synthesized CQDs decorated with SnO_2 (CQDs@SnO_2) and $NaVO_3$ (CQDs@$NaVO_3$) are used as anode and cathode materials in the fabrication of flexible SIBs. PVA-based poly(3-hexylthiophene) (P3HT) is used as the gel-polymer electrolyte in SIBs. The synthesized CQDs, forming the anode and cathode materials, are characterized through ultraviolet-visible (UV-vis) spectroscopy, Fourier transform infrared spectroscopy (FTIR), X-ray diffraction (XRD) study, scanning electron microscopy (SEM), energy-dispersive X-ray spectroscopy (EDS) and transmission electron microscopy (TEM). Various separators such as indium tin oxide coated polyoxyethylene tridecyl ether (ITO/PTE), rice paper (RP), silicone with three big holes (SIL BH), silicone with many small holes (SIL SH) and cellulose paper (CP) are tested in flexible batteries. The electrochemical performances of fabricated batteries are investigated by cyclic voltammetry. The charge–discharge profile is studied using chronoamperometry and the cyclability at 1 and 2 V is investigated using the chrono charge–discharge technique.

1 Materials and methods

1.1 Materials

The sodium metavanadate ($NaVO_3$), tin (II) chloride dehydrate ($SnCl_2.2H_2O$), polyvinyl alcohol (PVA), poly(3-hexylthiophene) (P3HT), indium-doped tin oxide/polyoxyethylene tridecyl ether (ITO/PTE) sheet (surface resistivity of 60 Ω/sq, 1 ft.L × 1 ft.W × 5 mil. thickness), 1-methyl-2-pyrrolidone anhydrous, polytetrafluoroethylene (Sigma-Aldrich), sodium hydroxide (NaOH), sulphuric acid (95–97%) (Merck), carbon black Vulcan XC-72 R (Fuel Cell Earth), hydrogen peroxide (40% m/v in water) (H_2O_2) (Carlo Erba reagents) and CP (CAT No:3001–845) (GE Healthcare UK Ltd) required for this study were acquired shortly before the commencement of the project. Dead leaves of the tree *S. saman* were collected from King Mongkut's University of Technology Thonburi, Bangkhuntien campus, Bangkok, Thailand. All other chemicals were used as received without any purification.

1.2 Preparation of CQDs from dead leaves of the tree *S. saman*

The dead leaves of the tree *S. saman* were separated from miscellaneous plant matter, cleaned with tap water, dried under sunlight, further dried in a hot-air oven at 80°C and powdered. The alkaline-peroxide-assisted hydrothermal carbonization method was followed in the synthesis of the CQDs. Initially, 3 g of leaf powder was mixed with 0.2 M sodium hydroxide solution (70 mL). Then, 10 mL of hydrogen peroxide solution was added into the above mixture. The mixture was stirred at room temperature for 2 h using a magnetic stirrer. It was then transferred into a 100-mL Teflon-lined autoclave and kept in a muffle furnace at 195 ± 5°C for 16 h. The autoclave was cooled naturally to reach room temperature. After completion of the reaction, the suspension was filtered through a Whatman filter paper (6 μm) to remove large amounts of hydrochar. The filtrate was further passed through a secondary filter paper (0.2 μm) to remove small particles. The resultant dark-brown carbonaceous (CQDs) solution was centrifuged at 10 000 r.p.m. for 30 minutes to get a clear solution.

1.3 Purification of CQDs

The solution obtained after centrifugation was washed using dichloromethane to remove any unreacted organic moieties. It was then transferred to a rotary evaporator (70°C, 600–200 mbar) to remove the water. The viscous form of the remnant was further dried in a hot-air oven at 60°C until the moisture was removed to the maximum. It (CQDs) was subsequently stored in a refrigerator at −30°C overnight and then freeze dried at −50°C, 1 mbar for 7 h to completely remove the moisture content. The solid form of CQDs were treated with absolute ethanol (99.9%) by shaking in a centrifuge tube [31]. The content was centrifuged to obtain solid CQDs. The solid CQDs were calcined in a tubular furnace at 700°C for 2 h under an N_2 atmosphere. The calcined CQDs (purified) showed solubility in distilled water and emitted a blue colour at 360 nm (Scheme 1).

1.4 Synthesis of tin oxide (SnO_2) nanoparticles

To synthesize the SnO_2 nanoparticles, 3 g of tin(II) chloride dihydrate ($SnCl_2.2H_2O$) was added with 0.2 M of NaOH (0.56 g of NaOH dissolved in 70 mL of distilled water) and 10 mL of H_2O_2. The content was stirred at room temperature (25°C) for 2 h. Then, it was transferred to a Teflon-lined autoclave and placed in a muffle furnace at 195 ± 5°C for 12 h. After completion of the reaction, the mixture was centrifuged at 10 000 r.p.m. at 25°C for 15 minutes. The solid was washed first with distilled water and then with ethanol. The purified material was dried in a hot-air oven at 75°C and calcined at 500°C for 2 h in a muffle furnace to obtain pure SnO_2 nanoparticles.

1.5 Synthesis of CQD-decorated SnO_2 nanoparticles (anode)

The supernatant liquid of CQDs (20 mL) (Section 1.2) was added with ethanol (10 mL). It was mixed with 0.5 g of synthesized SnO_2 nanoparticles. The suspension was stirred at room temperature for 2 h and dried in a hot-air oven at 60°C to evaporate the moisture. The CQD-decorated SnO_2 nanoparticles thus obtained were calcined at 700°C for 2 h under an N_2 atmosphere. The calcined material was used in the fabrication of the anode.

1.6 Synthesis of CQD-decorated $NaVO_3$ nanoparticles (cathode)

CQD-decorated $NaVO_3$ nanoparticles were prepared as per the procedure contained in Section 1.5. The synthesized material was used in the fabrication of the cathode.

1.7 Synthesis of gel-polymer electrolyte PVA/P3HT

PVA (1 g) was dissolved in 10 mL distilled water to which 1 g of concentrated H_2SO_4 was added. The mixture was heated (85°C) and stirred for 2 h to form a gel [32]. A solution containing 50 mg poly(3-hexylthiophene) (P3HT) dissolved in

3 mL of chloroform was added to the above PVA gel. Then, it was stirred at 40°C for 30 minutes to get a black-coloured gel.

1.8 Materials characterizations

A UV-vis spectrometer (Biotek), FTIR spectrometer (Thermo Nicolet Corporation), XRD using Ni-filtered Cu $K\alpha$ radiation (v = 1.54 A°) at 40 kV and 40 mA (Rigaku RINT 2100), SEM (JEOL, JSM-6610LV), TEM (JEOL JEM 2100-Plus 200 kV) and EDS (INCA-xart) were employed to characterize the optical properties, morphology, size, structure and composition of the synthesized materials.

1.9 Fabrication of flexible SIBs

A schematic diagram of the design details of a flexible battery are presented in Fig. 1a and b. The active material ($CQDs@SnO_2$ or $CQDs@NaVO_3$) in powder form was mixed well with conductive carbon black Vulcan XC-72R and polytetrafluoroethylene (weight ratios of 70:25:5) in 1-methyl-2-pyrrolidone using a vortex. The mixture was kept for 48 h at room temperature to form a homogeneous slurry. The slurry was coated on the ITO/PTE (2 cm × 1 cm, 5 mil. thickness) using the doctor blade technique. The coated substrate was dried at 50°C for 2 h. The current collector copper sheet (0.1 mm thickness) was

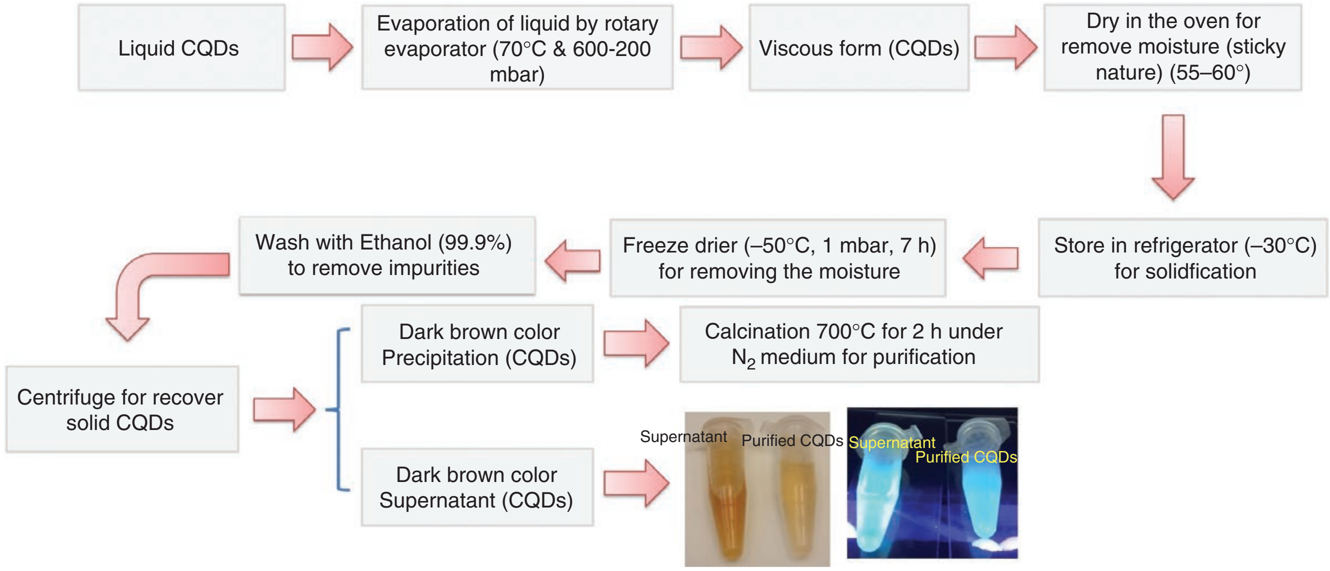

Scheme 1: The processing steps for the preparation of purified solid CQDs from liquid CQDs

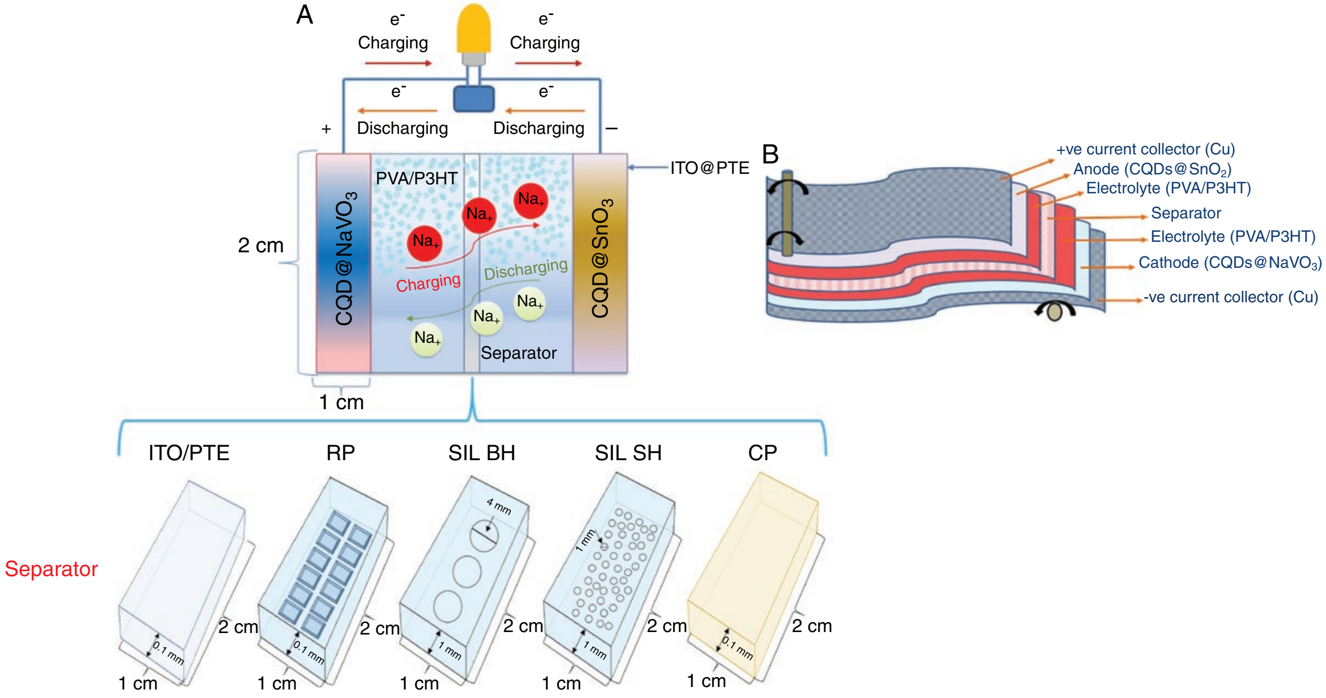

Fig. 1: Schematic diagram of (a) a battery using various separators and (b) the design of a flexible battery

tightly pressed onto the surface of anode and cathode up to a distance of 1 cm from the edge of the substrate to get a good electrical contact. PVA/P3HT was used as a gel-polymer electrolyte. Various separators: ITO/PTE (0.1-mm thickness, area: 2 cm^2), RP (0.1-mm thickness, area: 2 cm^2), SIL BH (1-mm thickness with three holes of 4-mm dia. each, area: 2 cm^2), SIL SH (1-mm thickness with many holes of 1-mm dia. each, area: 2 cm^2) and CP (0.1-mm thickness, area: 2 cm^2) were investigated. The separator was dipped well into the gel-polymer electrolyte with the anode surface rested in it for a few minutes. The cathode was then placed on the top side of the separator. The edges were sealed using sticky tape so as to prevent leakage of the electrolyte. Further, the battery was shielded well with three layers of white paper masking tape to avoid air contact. The fabricated batteries were preserved in a closed container.

1.10 Electrochemical studies

The electrochemical storage properties of cyclic voltammograms (0–3.5 V vs Na/Na^+, 0.5 mV s^{-1}), charge–discharge performances by chronoamperometry (1–2.5 V) and chrono charge–discharge (50 cycles) in different potential voltages at room temperature using an Autolab (AUT 86930) were investigated. The electrochemical impedance spectra (EIS) were studied in a frequency ranging from 0.1 Hz to 0.1 MHz at an open-circuit potential of 0.02 V.

2 Results and discussion

2.1 Synthesis of CQDs by alkaline-peroxide-assisted HTC

The alkaline-peroxide-assisted hydrothermal carbonization method is used to synthesize CQDs from cleaned and dried leaves of the tree S. *saman*. Major chemical compositions of the leaves under study are crude protein 22.6%, neutral detergent fibre 47.5% and acid detergent fibre 36.9% [33]. The dead-leaves powder was pre-treated with alkaline-peroxide solution. The above was processed in HTC to get CQDs. The procedure for synthesizing CQDs from dead leaves and its morphology and fluorescence are presented in Scheme 2. The dead leaves were passed through hydrolysis, dehydration, decarboxylation, condensation, polymerization and aromatization followed by a hydrothermal carbonization process so as to obtain smaller monomers [34–36].

Alkaline-hydrogen-peroxide treatment is a simple procedure to enhance the properties of CQDs. This method is widely used in delignification and bleaching in the pulping industry through the oxidation of hydrogen peroxide. Hydrogen peroxide dissociates with sodium hydroxide to form hydroperoxyl (HOO^-) ions ($H_2O_2 + OH^- \leftrightarrow H_2O + HOO^-$). The hydroperoxyl ions act as a strong oxidant that enhances the yield of quantum dots with abundant functional groups on the surface. On increasing the concentration of NaOH–H_2O_2 within the optimum level, the particle size tends to decrease. Beyond the optimum concentration, the particle size increases dramatically by aggregation [36, 37]. NaOH (70 mL of 0.2 M solution) and 10 mL of H_2O_2 were used in this study. Alkaline-peroxide-assisted hydrothermal carbonization offers Na-doped CQDs to enhance sodiation/desodiation during the charging and discharging processes in SIBs.

2.2 Characterizations of synthesized materials

The absorption and emission spectra of the purified CQDs are presented in Fig. 2a–g. The absorbance at 285 nm is due to π–π* transitions by the aromatic C=C bond in the core.

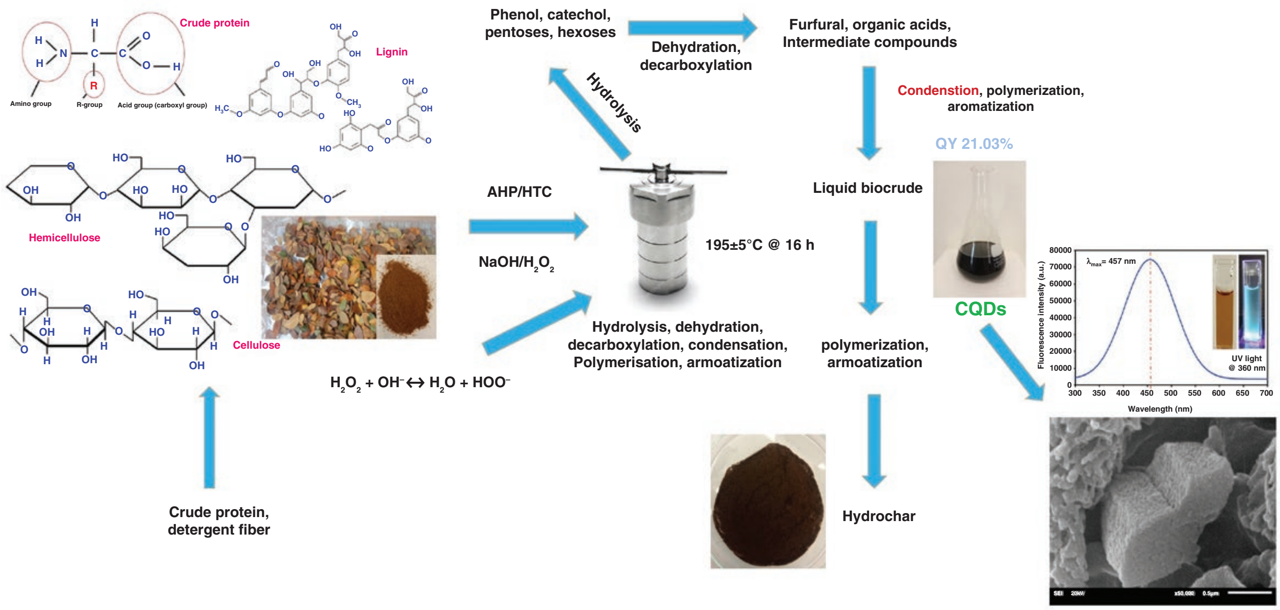

Scheme 2: The synthesis mechanism of CQDs from dead leaves and their properties of fluorescence and morphological structure

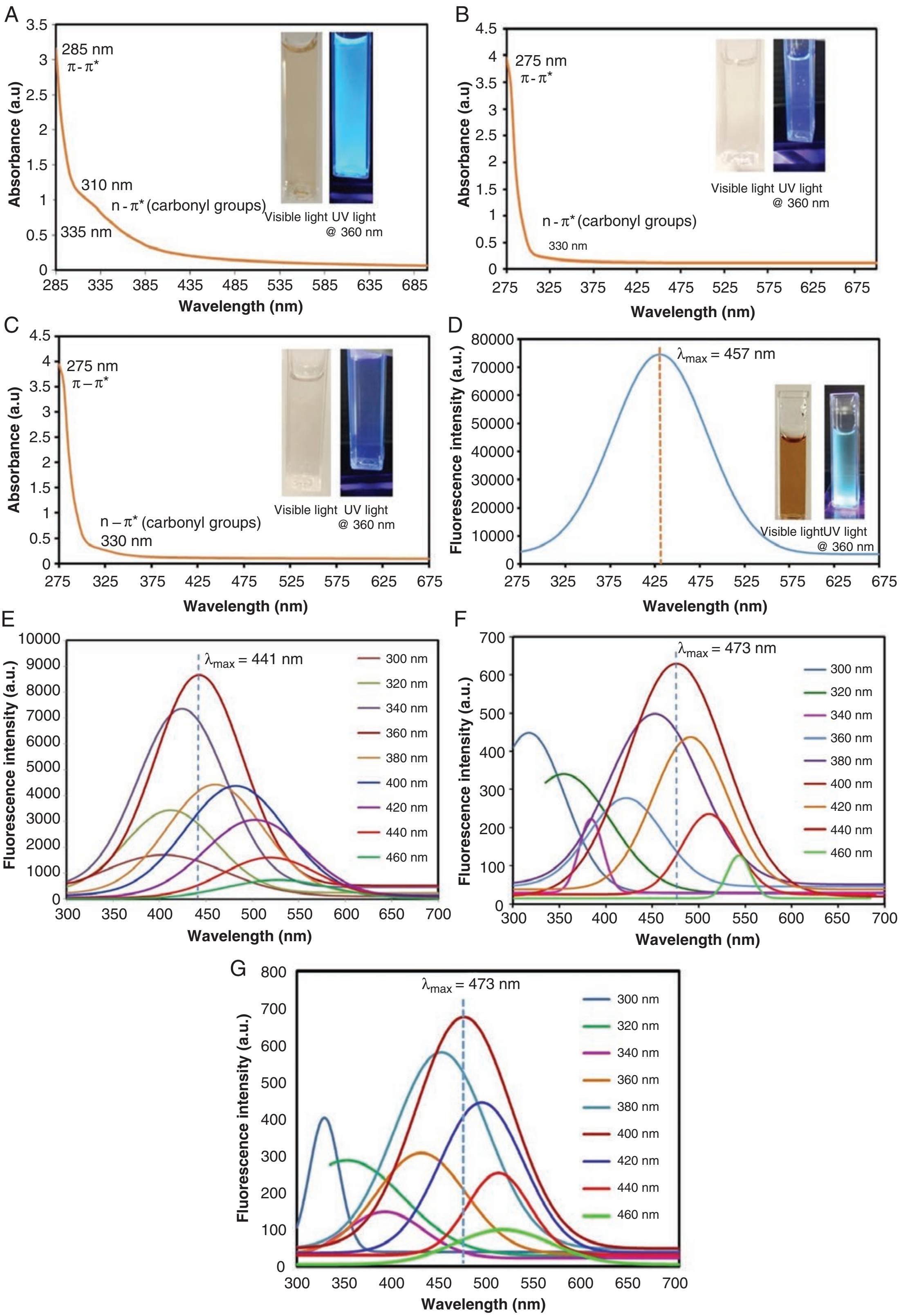

Fig. 2: UV-vis spectra of prepared materials. Absorbance spectra of (a) CQDs, (b) CQDs@SnO_2, (c) CQDs@$NaVO_3$; (d) fluorescence spectrum of CQDs at 360 nm; fluorescence spectrum of CQDs at different excitation wavelengths of (e) CQDs, (f) CQDs@SnO_2 and (g) CQDs@$NaVO_3$.

A broad shoulder at 335 nm reveals that the *n*–π* transition occurs by C=O from the surface of CQDs (Fig. 2a). Variations do occur in the absorbance spectrum of CQDs decorated with SnO_2 and $NaVO_3$ (Fig. 1b and c). CQDs exhibit a maximum emission wavelength of 457 nm at the excitation wavelength of 360 nm. However, on increasing the excitation wavelength from 380 to 460 nm with an increment rate of 20 nm, the intensity of the emission decreases gradually, as shown in Fig. 2d. The synthesized CQDs emit strong blue-coloured radiation while CQD-decorated SnO_2 and CQD-decorated $NaVO_3$ emit a weak blue colour at 360 nm (Fig. 2a–c). The emission is known to be influenced by various defects such as the size and functional groups on the surface of the CQDs. The quantum yield of CQDs is calculated to be 21.03% by quinine sulphate as the reference, which is in line with earlier works (Table 1).

The quantum yield is in accordance with the concentration of HOO^-, which in turn relies on the concentrations

Table 1: Comparison of quantum yield (QY) and size of CQDs from various biomass sources

Biomass	Method	Reaction conditions	Size (nm)	QY	Reference
Azadirachta indica leaves (paste)	Hydrothermal carbonization (HTC)	Temp. 150°C for 4 h	3.2	27.2	[39]
Oriental plane leaves (deciduous, broad leaves), lotus leaves (hydrophytes) and pine needles	Pyrolysis	NA	3.7	16.4 (oriental plane) 15.3 (lotus) 11.8 (pine)	[40]
Mint leaves	HTC	Temp. 200°C for 5 h	4–9	7.64	[41]
Bamboo leaves	HTC	Temp. 200°C for 6 h	NA	7.1	[42]
Glucose	HTC	Temp. 200°C for 6 h	NA	4.03	[37]
Glucose	Pyrolysis	250°C, 2 h	NA	14.9	
Glucose	HTC and alkaline-peroxide treatment	Temp. 200°C for 6 h (HTC) and 0.3 M/2.4 wt% of NaOH and H_2O_2 (alkaline-peroxide treatment)		22.67	
Purple perilla	HTC	Temp. 260°C for 5 h	2.8	9.01	[43]
Samanea saman (Rain tree) dead leaves	Alkaline-peroxide-treatment-assisted HTC	Alkaline-peroxide treatment (0.2 M/10 mL) for 2 h at RT and HTC (195 ± 5°C for 16 h)	4.00 ± 0.964	21.03	This study

[a]Temp., temperature; NA, not available.

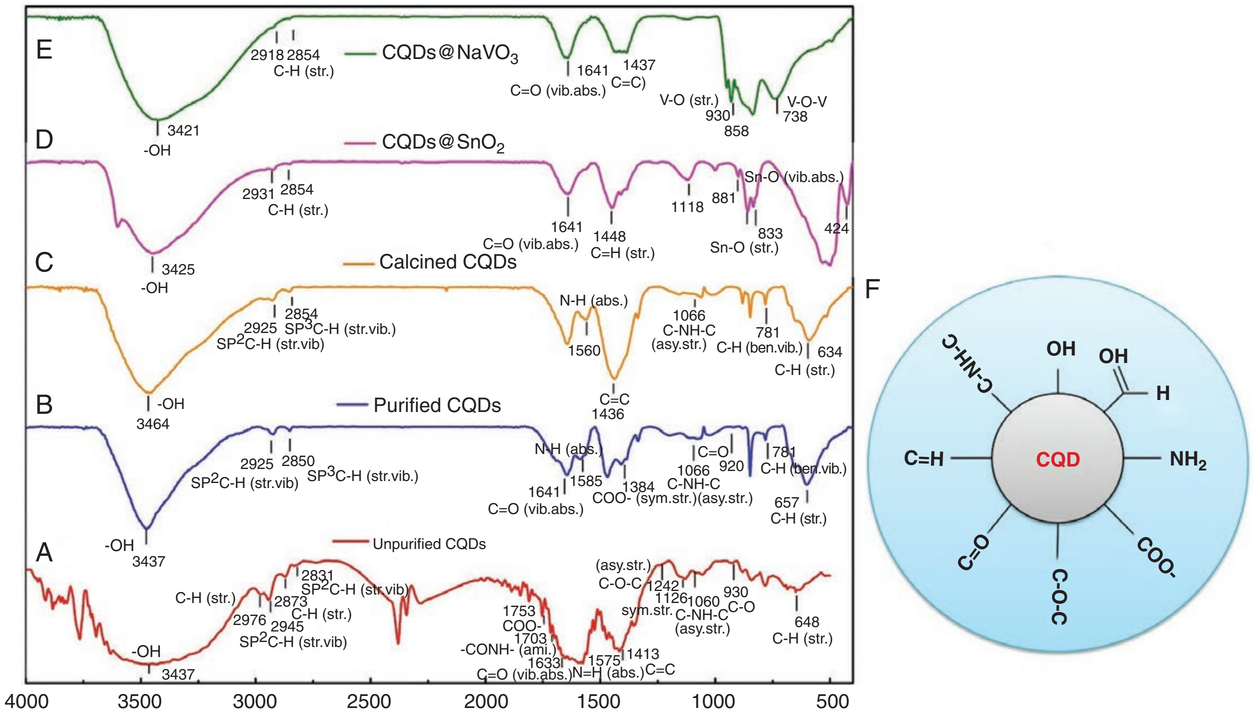

Fig. 3: FTIR spectra of (a) unpurified CQDs, (b) purified CQDs, (c) calcined CQDs, (d) CQDs@SnO_2, (e) CQDs@$NaVO_3$ and (f) functional groups on the surface of CQDs

of NaOH and H_2O_2 [37]. Fig. 2e–g show the excitation-dependent emission spectra of CQDs. The emission peak gradually shifts from short to long wavelength on increasing the excitation wavelength from 300–460 nm. The maximum emission wavelength varies from the blue to the green region (440 to 540 nm). This bathochromic shift, which depends on the emission wavelength, decreases in fluorescence intensity. This reveals that the CQDs have ketonic, carbonyl and hydroxyl functional groups as indicated by the FTIR spectra (Fig. 3a and b). In addition, the excitation-dependent emission is related to the anti-stokes emission and surface-energy trap of CQDs that give forth blue-coloured radiation under UV light [37, 44]. The different excitation wavelengths may cause consecutive excited energy distributions, charge separation, electron confinement and holes on the surface of CQDs [45, 46].

The FTIR spectra of unpurified CQDs, purified CQDs and calcined CQDs along with those of CQD-decorated SnO_2 and CQD-decorated $NaVO_3$ are presented in Fig. 3a–e. The bands at 630–660 cm^{-1} are attributed to the stretching vibration of C–H. The band at ~1060 cm^{-1} reveals the asymmetric stretching mode of C–NH–C. Peaks associated with the stretching vibration modes of carboxyl (–COOH) and hydroxyl (–OH) are at ~1753 and ~3437 cm^{-1}, respectively. The characteristic peaks at ~2854 and ~2925 cm^{-1} are assigned to the stretching vibration modes of *sp*^{3} and *sp*^{2} C–H, respectively [47]. The peaks at 1400 to 1450 cm^{-1} correspond to the C=C stretching vibration. The absorbance vibrational mode of C=O is identified at the peaks at ~1630–1640 cm^{-1} [48]. The functional groups of CQDs are eliminated by purification (Fig. 3b) as confirmed by that of the unpurified CQDs (Fig. 3a). The calcined CQDs have limited functional groups (Fig. 3c) as compared to those of purified and unpurified CQDs due to calcination at high temperature that eliminates several functional groups. The solubility of CQDs in water is in the order of unpurified CQDs > purified CQDs > calcined CQDs due to the number of functional groups present on the surface of CQDs. The peaks at 424 and 833 cm^{-1} reveal the presence of absorbance and stretching bands of Sn–O (Fig. 3d). The stretching vibration bands of V–O–V and V–O occur at 738 and 930 cm^{-1}, respectively (Fig. 3d). CQD-decorated SnO_2 and $NaVO_3$ have absorbance and stretching vibration bands of C=O and C–H (Fig. 3d and e).

The XRD patterns of the uncalcined CQDs, calcined CQDs, CQD-decorated SnO_2 and CQD-decorated $NaVO_3$ are presented in Fig. 4a–d. A dominant peak at 26° and a small peak at 23° appear in all the materials that correspond to the crystalline planes of (0 0 2) and (1 2 0) diffraction of disordered carbonaceous structure with interlayer spacing of 0.33 and 0.37 nm. Uncalcined CQDs express small peaks at 18°, 29°, 34°, 46° and 54° corresponding to (1 0 3), (3 0 0), (1 2 3), (1 0 0) and (0 1 3) diffraction planes, which indicates that carbon remains at random (Fig. 4a). CQDs are known to contain many oxygen-holding groups on the surface, which is consistent with EDS data [44]. Two small peaks (18° and 46°) are absent in calcined CQDs as high-temperature calcination eliminates the peaks (Joint Committee on Powder Diffraction Standards (JCPDS) number: 75–1621, 50–1082, 50–0926, 75–0444, 48–1206, 22–1069) (Fig. 4b). The diffraction planes (2 0 0), (1 0 3), (1 2 0), (4 0 0), (2 0 1), (5 0 1) and (0 1 2) identified in CQDs@$NaVO_3$ are attributed to $NaVO_3$ (JCPDS number: 32–1197, 89–9051) (Fig. 4d). The CQDs of d-spacing are found (0.37 nm) using the JCPDS database, which is consistent with TEM data. In addition, CQDs have a hexagonal structure that is consistent with the SEM image (Fig. 5b). The peaks at 34°, 38°, 52° and 55° correspond to the (1 1 0), (1 1 1), (2 0 1) and (2 2 0) diffraction planes of SnO_2 (JCPDS number: 41–1445, 85–0712, 72–2324). It suggests the purity of SnO_2 (Fig. 4c). The average crystalline size of uncalcined CQDs, calcined CQDs, CQDs@SnO_2 and CQDs@$NaVO_3$ are calculated to be 12.8, 11.5, 11.9 and 14.4 nm, respectively, through Scherer's equation.

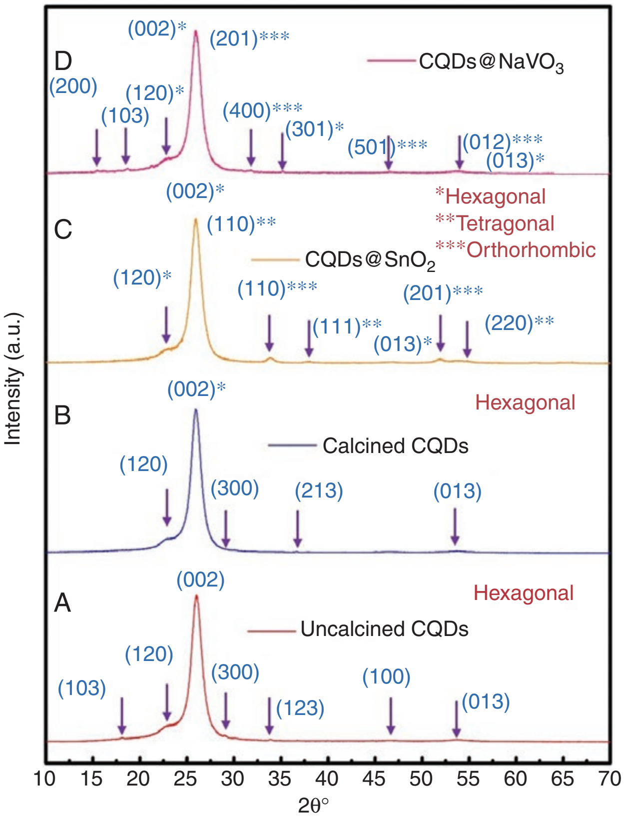

Fig. 4: XRD patterns of (a) uncalcined CQDs, (b) calcined CQDs, (c) CQDs@SnO_2 and (d) CQDs@$NaVO_3$

Morphological studies of uncalcined CQDs, calcined CQDs, CQDs@SnO_2 and CQDs@$NaVO_3$ were investigated using SEM (Fig. 5a–d). The morphological structure of CQDs obtained from the dead leaves of *S. saman* is shown in Fig. 5a. Protein is known to be in the form of crystalline nanorods in synthesized calcined CQDs. Neutral detergent fibre and acid detergent fibre form flakes when agglomerated. Calcined CQDs are crystalline (Fig. 5b) when compared to uncalcined CQDs (Fig. 5a) due to the effect of high temperature (700°C)

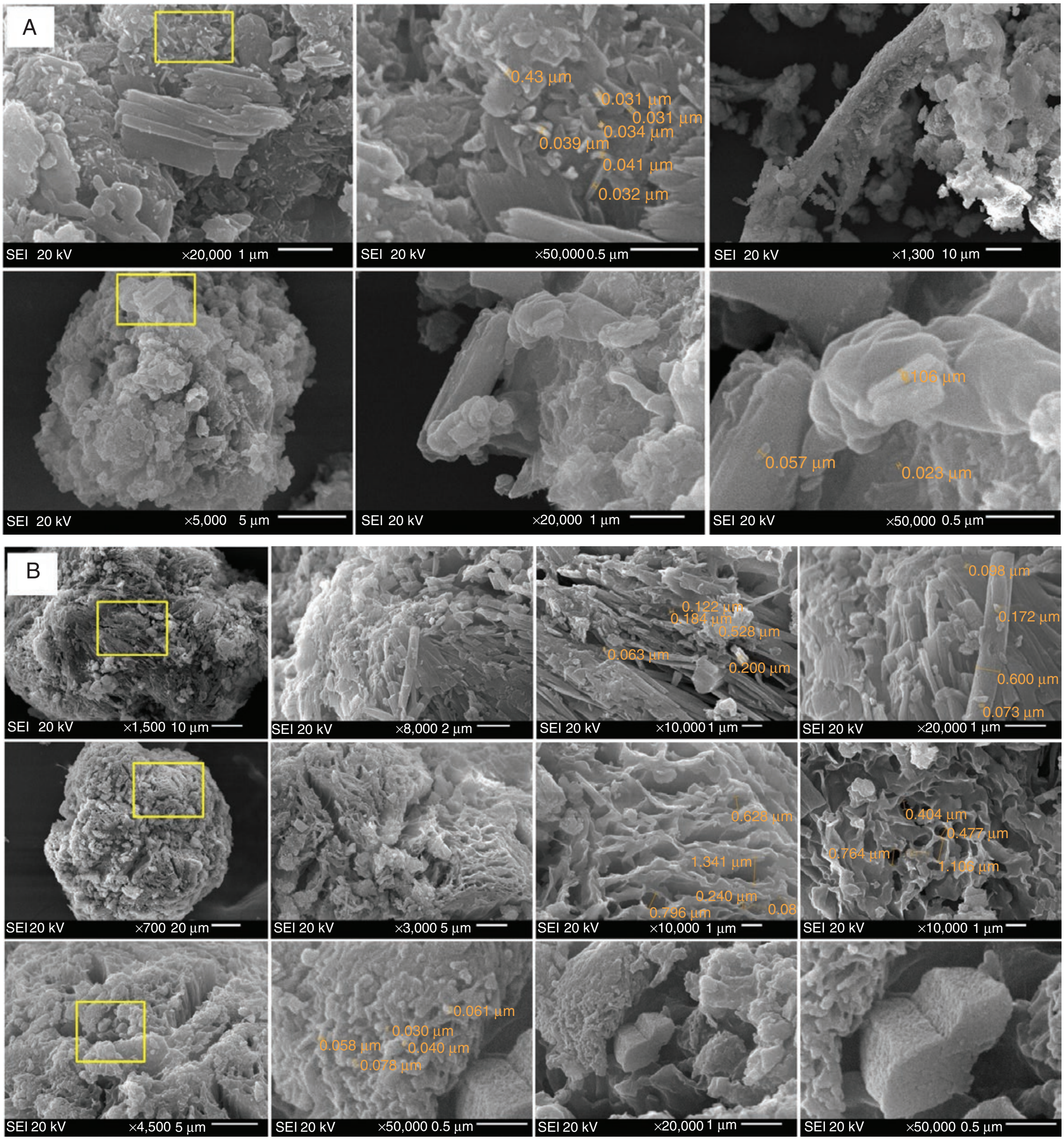

Fig. 5: SEM images of (a) uncalcined CQDs, (b) calcined CQDs, (c) calcined CQDs@SnO_2 and (d) calcined CQDs@$NaVO_3$

under an N_2 atmosphere. In addition, a porous consistency is formed in the detergent fibre of the calcined CQDs (Fig. 5b). A hexagonal structure appears on calcined CQDs (Fig. 5b), which is in relation to the XRD pattern (Fig. 4b) and also with the TEM images of CQDs@SnO_2 (Fig. 7a and b). CQD-decorated SnO_2 appears as nanorods due to agglomeration (Fig. 5c). CQD-decorated $NaVO_3$ appears like a tree with roots and branches. Nanosized crystalline particles of CQDs are seen on the rod-shaped roots, which may be a vanadium compound of $NaVO_3$. CQDs from fibre materials are flake-shaped with differently sized pores (Fig. 5d).

The elemental composition of synthesized materials was analysed using the EDS technique (Fig. 6). Uncalcined as well as calcined CQDs mainly consist of C, O and Na, which reveals that the CQDs are made up of an oxygenous carbon structure. Both the materials contain higher oxygen than carbon due to NaOH and H_2O_2, which offer relatively high specific capacitance and rate capability (Fig. 6a and b). Na is present in these synthesized materials, since the alkaline-peroxide (NaOH–H_2O_2)-assisted hydrothermal carbonization is being used in the preparation. CQD-decorated SnO_2 has high amounts of Sn (60.14%) and

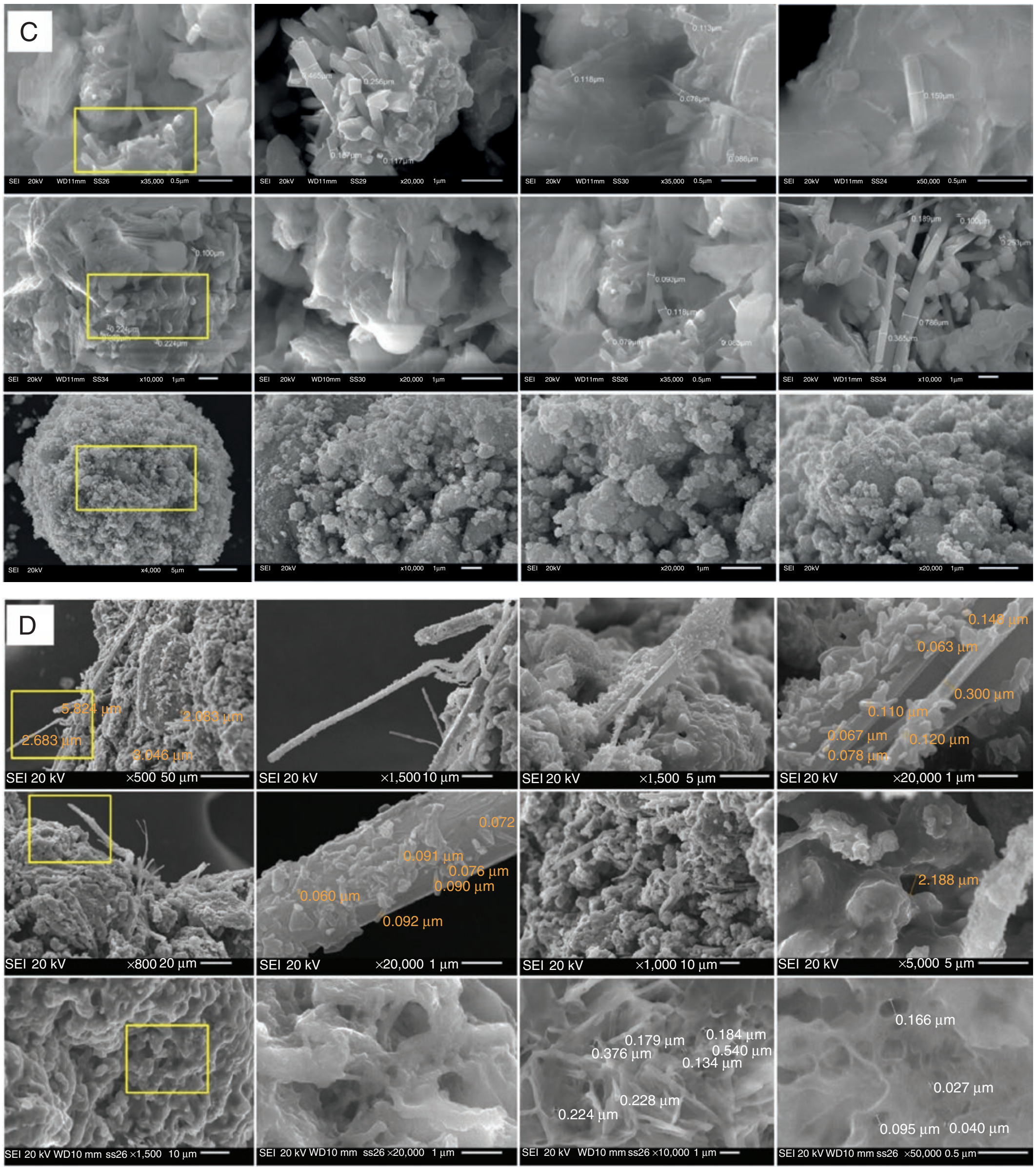

Fig. 5: Continued.

O (31.03%) (Fig. 6c). The cathodic material (CQDs@NaVO$_3$) mainly consists of V (35.99%) and O (38.61%) (Fig. 6d).

The morphology and structure of calcined CQDs, CQDs@SnO$_2$ and CQDs@NaVO$_3$ were investigated using TEM (Fig. 7a–c). The mean diameter of the calcined CQDs is 4.0 ± 0.96 nm ($n = 20$) (Fig. S1a in the online Supplementary Data). Selected area (electron) diffraction (SAED) of calcined CQDs exhibits a hexagonal lattice structure with different crystalline planes (1 0 3) and (1 2 3) that are in agreement with the XRD pattern and SEM of calcined CQDs. In addition, the distance between the two lattice points is 3.82 nm. Calcined CQDs are <10 nm in size and have many crystalline planes (2 0 1), (1 0 0), (0 0 2) and (3 0 0) with interlayer spacing of 0.371, 0.301, 0.340 and 0.306 nm. In addition, CQDs have the regular arrangement of carbon atoms (Fig. 7a). The yellow-coloured figures are the magnification of the Digital Micrograph software for calculating the values of *d*-spacing of the crystalline planes (Fig. 7b and c). CQDs derived from dead leaves have an interlayer spacing of 0.371 nm, with a high surface area, large interior voids and shortened mass or charge transportation lengths that effectively improve the specific capacity, rate capability and cycling stability of the SIBs [19, 48,49].

The diameter of CQDs@SnO$_2$ ranges from 2.11 to 10.75 nm with an average of 6.37 ± 2.15 nm ($n = 43$) (Fig. S1b in the online Supplementary Data). The particles are seen agglomerated with many crystalline lattice planes. The lattice fringes of these particles are distinct with interlayer spacing of 0.390 and 0.335 nm corresponding to the planes of (1 2 0) and (1 1 0) representing the CQDs and SnO$_2$, respectively. SAED reveals that the planes of SnO$_2$ (0 0 2) and (1 1 0) and CQDs (1 2 3) and (0 0 2) agree with the pattern of

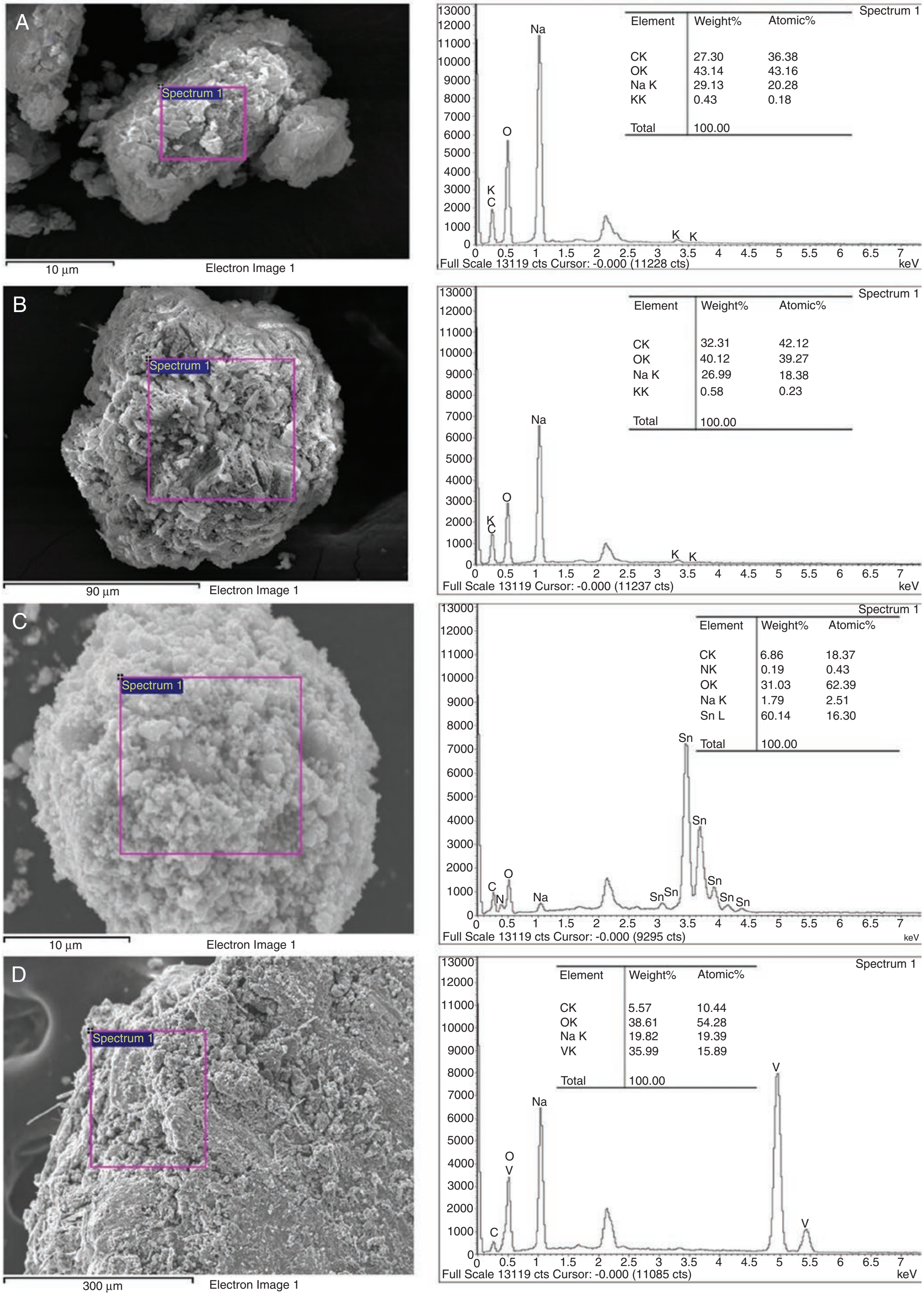

A — Spectrum 1

Element	Weight%	Atomic%
CK	27.30	36.38
OK	43.14	43.16
Na K	29.13	20.28
KK	0.43	0.18
Total	100.00	

B — Spectrum 1

Element	Weight%	Atomic%
CK	32.31	42.12
OK	40.12	39.27
Na K	26.99	18.38
KK	0.58	0.23
Total	100.00	

C — Spectrum 1

Element	Weight%	Atomic%
CK	6.86	18.37
NK	0.19	0.43
OK	31.03	62.39
Na K	1.79	2.51
Sn L	60.14	16.30
Total	100.00	

D — Spectrum 1

Element	Weight%	Atomic%
CK	5.57	10.44
OK	38.61	54.28
Na K	19.82	19.39
VK	35.99	15.89
Total	100.00	

Fig. 6: Elemental compositions of (a) uncalcined CQDs, (b) calcined CQDs, (c) CQDs@SnO_2 and (d) CQDs@$NaVO_3$

the XRD. The interlayer spacing of CQDs with a hexagonal structure is 0.33 nm, which corresponds to a lattice plane of (0 0 2) (Fig. 7b) [50]. The SAED pattern of CQDs@$NaVO_3$ shows a spherical structure with an interlayer spacing of 0.259 and 0.155 nm corresponding to the planes of (3 1 0) and (1 0 3) representing $NaVO_3$ and CQD at 35°C and 59°C (Fig. 7c). The surface of the CQDs@$NaVO_3$ has many crystalline planes with different interlayer spacing of 0.292,

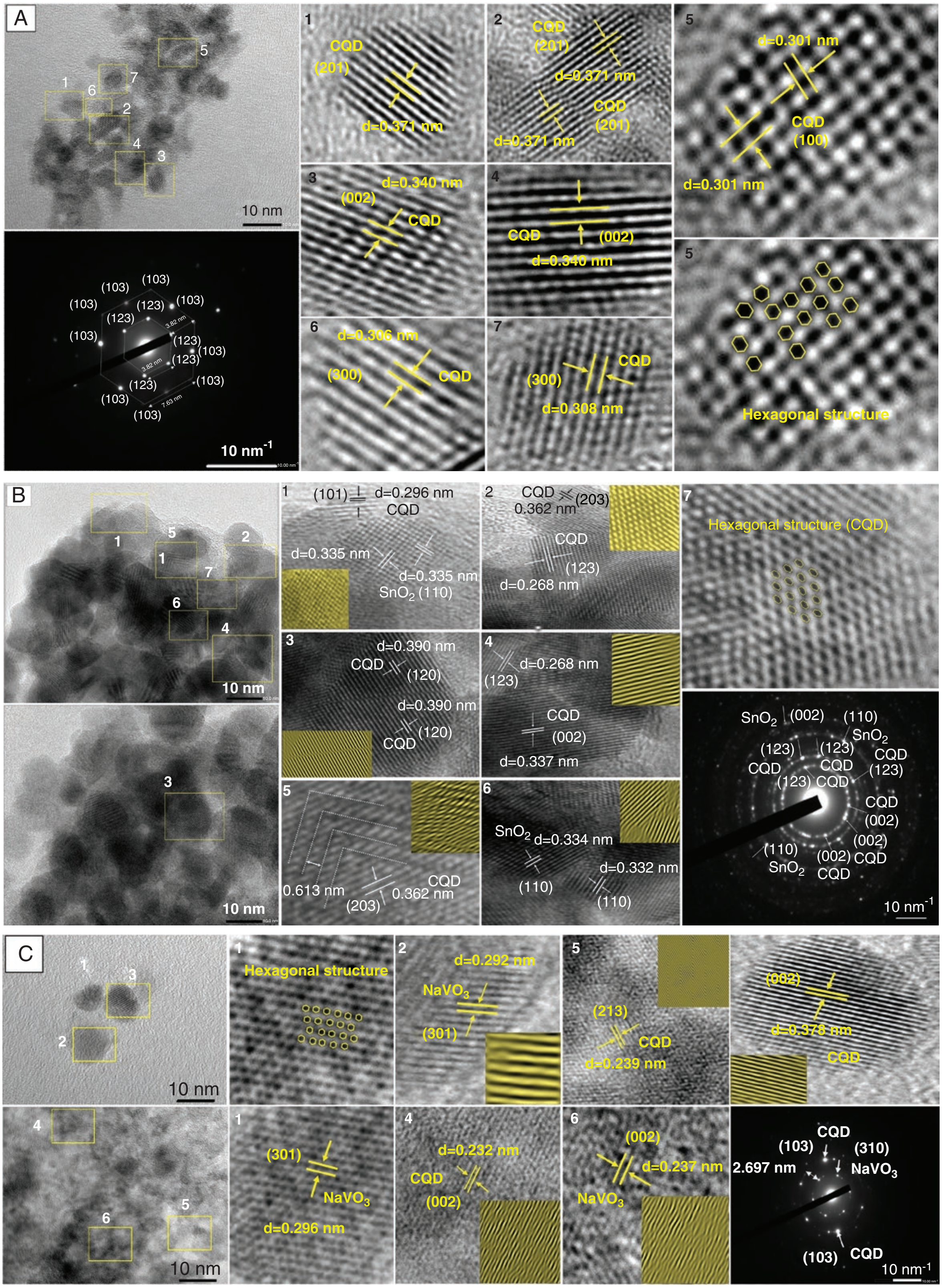

Fig. 7: TEM images of (a) calcined CQDs, (b) calcined CQDs@SnO$_2$ and (c) calcined CQDs@NaVO$_3$

0.239, 0.378 and 0.296 nm corresponding to the planes of (3 0 1), (2 1 3), (0 0 2) and (3 0 1), respectively, which remains consistent with the XRD pattern of CQDs (Fig. 4a and b) and CQDs@NaVO$_3$ (Fig. 4d). The Na-ion is larger (1.02 Å) than the Li-ion (0.76 Å), causing difficulty in intercalating them into graphite due to the short interlayer distance of graphite (~0.34 nm) [20, 51, 52]. Biomass-derived CQDs with a porous structure are chosen in this study so as to

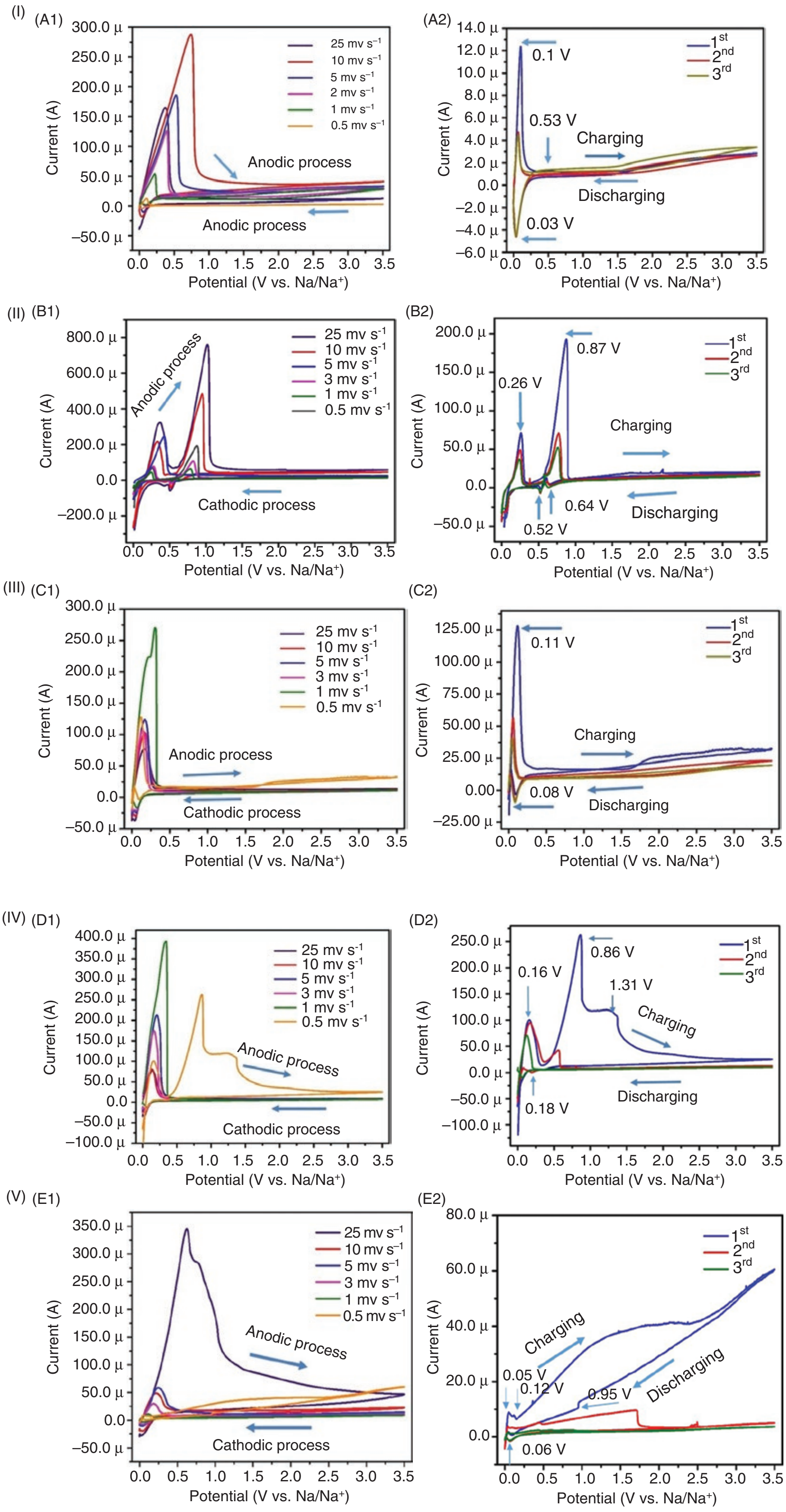

Fig. 8: Cyclic voltagrams of various separators in SIBs at various scan rates (0.5–25 mV s⁻¹) and the redox performance behaviour at 0.5 mV s⁻¹ (three cycles) (I) ITO/PTE (a1, a2), (II) RP (b1, b2), (III) SIL BH (c1, c2), (IV) SIL SH (d1, d2) and (V) CP (e1, e2)

overcome the problems caused by graphite due to its large interlayer distance coupled with a disordered structure. Synthesized CQDs@SnO_2 and CQDs@$NaVO_3$ facilitate the intercalation of Na-ions efficiently during the charging and discharging processes due to the large interlayer distances of 0.39 and 0.378 nm.

2.3 Electrochemical performances of flexible Na-ion batteries

The cyclic voltammetry (CV) of the fabricated batteries using different separators was studied at various scan rates (25, 10, 5, 3, 1 and 0.5 mV s^{-1}) and in three initial cyclic CVs at 0.5 mV s^{-1} within the potential range of 0–3.5 V in order to characterize the performance of the batteries (Fig. 8I–V). The capacitance values are high at low scan rates. The CVs of batteries show peaks arising from reversible oxidation and reduction reactions at various scan rates. Peaks are formed by the Na-ion insertion and extraction in the CQDs together with the gel-polymer electrolyte [53]. In the ITO/PTE separator, the oxidation peaks at 0.1 and 0.53 V, corresponding to the reduction peak at 0.03 V, appear in the first cycle whereas the oxidation peak at 0.53 V disappears in the subsequent cycles. In addition, the height of the oxidation and reduction peaks is seen as reduced in the second and third cycles, even when the current is reduced. The CV curves of the second and third cycles overlap indicating a good cycling performance of CQDs with porous structured anode and cathode materials during sodiation and desodiation processes [10]. The anodic peak at 0.1 V originates from the reversible sodiation/desodiation process [54] (Fig. 8I a2). In addition, there is no distinct peak indicating the decomposition of the electrolyte and it may be seen that the second and third cycles are superimposed. It reveals that there is no solid electrolyte interface (SEI) formed on the electrode surface and most of the Na-ions are reversibly drawn into the CQDs [55].

In the case of RP as the separator in SIBs, there are two oxidation peaks at 0.26 and 0.87 V and reduction peaks at 0.52 and 0.64 V, respectively. This battery releases a higher current by oxidation peaks than the ITO/PTE separator whereas the reduction peaks have low current values (Fig. 8II b2). The area of the reduction peaks is lower than that of the oxidation peaks. The two irreversible reduction peaks at 0.52 and 0.64 V in all the cycles reveal that there is no formation of SEI. The reversible reduction peaks at 0.52 and 0.64 V are attributed to Na-ion insertion–extraction in the interlayers of the CQDs [56]. The SIL BH separator in SIBs has oxidation (0.11 V) and reduction (0.08 V) peaks (Fig. 8I II c2) whose response is similar to that of the ITO/PTE separator. But, the reduction peak of SIL BH releases a current lower than that of ITO/PTE. In the case of SIL SH, the CV of the separator shows three oxidation peaks at 0.16, 0.86 and 1.31 V (Fig. 8I V d2) when compared to SIL BH. The irreversible reduction peaks occur at 0.3, 0.18 and 0.06 V in the consecutive three cycles. The study reveals that the holes on the surface of silicone influence the performance of the batteries. Silicone with many small holes (SIL SH) has a higher amount of gel loading than that of silicone with larger holes (SIL BH). In SIBs with CP as the separator, two anodic peaks are formed at 0.05 and 0.12 V in all the cycles. But, the cathodic peak of the first cycle at 0.1 V and the second and third cycles of the cathodic peak formed at 0.06 V are superimposed (Fig. 8V e2).

The specific capacitance value of fabricated batteries is calculated from the following formula using a mathematical area (Equation 1) for the CV curve at a scan rate of 0.5 mV s^{-1}:

$$\text{Specific capacitance}\left(\mathrm{F\ g^{-1}}\right) = \frac{\int Idv}{m \times v \times (v_f - v_i)} \tag{1}$$

where $\int Idv$ denotes the integral area under the CV curve, m is the mass of the active material on the surface of the working electrode (g), v is the scan rate (0.5 mV s^{-1}) and $(v_f - v_i)$ is the functional potential window (V).

The specific capacitance value of the batteries ITO/PTE, RP, SIL BH, SIL SH and CP are 13, 266, 116, 881 and 183 F g^{-1}, respectively. SIL SH has achieved a higher specific capacitance (881 F g^{-1}) than SIL BH (116 F g^{-1}) due to the number and size of the holes on the surface of the flexible silicone sheet. SIL SH may have higher amount of gel-polymer electrolyte than SIL BH. The capacitance values of SIL SH are higher at low scan rates than at higher scan rates and are near to the ideal shape. While charging all batteries at 0.5 mV s^{-1} from zero potential, the current initially increases and then decreases as the electric potential is increased expressing a *hump* in the CV curve [57, 58].

Charge–discharge studies made using chronoamperometry for fabricated batteries at 1, 1.5, 2 and 2.5 V for 1 h are presented in Fig. 9I–V and the data of its origin are shown in Fig. S2I–IV in the online Supplementary Data. The specific capacitance of fabricated batteries is calculated from the charge and discharge profile as shown in Equation 2:

$$\text{Specific charge or discharge capacity}\left(\mathrm{mC\ g^{-1}}\right) = \left[\frac{0.5 \times (t_2 - t_1) \times (i_2 + i_1)}{m}\right] \times 10^3 \tag{2}$$

where $(t_2 - t_1)$ denotes the time duration (s), $(i_2 + i_1)$ denotes is the charge (C) and m refers to the mass of the active material on the surface of working electrode (g).

On increasing the potential from 1.0 to 2.5 V, the specific discharge capacities increase in the ITO/PTE separator. But the specific charge capacity is low at high voltages (Fig. 9I). RP as a separator has a high specific discharge capacity at high voltages of 2.0 and 2.5 V but it has poor charge and discharge capacities at 1–1.5 V (Fig. 9II). CP has high specific charge capacities at high voltages (1 and 1.5 V) whereas the discharge capacity gradually increases on increasing the voltage (Fig. 9V). Both the silicone separators delivered higher specific charge and discharge capacities at 1 and 2 V than those of other separators (Fig. 9III and IV). However, the specific discharge capacities

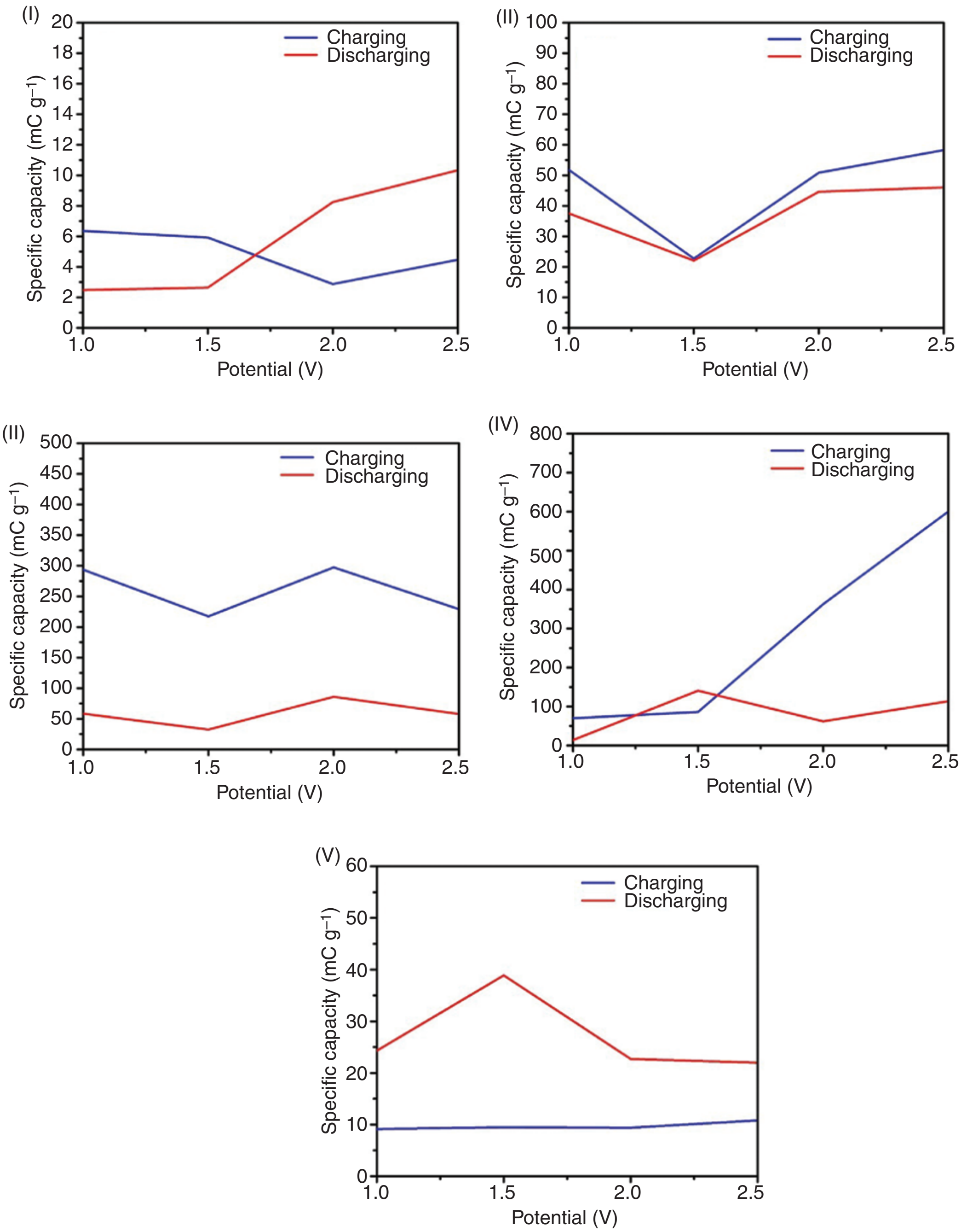

Fig. 9: Charge–discharge capacity profile of SIBs using various separators at different voltages (I) ITO/PTE, (II) RP, (III) SIL BH, (IV) SIL SH and (V) CP

are lower than the specific charge capacities due to poor desodiation at 1 V. At 1.5 V, SIL SH delivered a higher specific discharge capacity (141 mC g^{-1}) than SIL BH (32 mC g^{-1}). RP delivered a specific charge capacity of 23 mC g^{-1} and a discharge capacity of 22 mC g^{-1} at 1.5 V. CP has a specific discharge capacity of 39 mC g^{-1} at 1.5 V. SIL SH delivered a specific charge capacity of 600 mC g^{-1} and a discharge capacity of 114 mC g^{-1} at 2.5 V. The specific charge capacities of SIL BH in SIBs are 294, 217, 297 and 229 mC g^{-1} at 1.0, 1.5, 2.0 and 2.5 V, respectively, whereas the corresponding specific charge capacities of SIL SH are 70, 87, 363 and 600 mC g^{-1}. SIL SH delivers a maximum discharge capacity of 141 and 114 mC g^{-1} at 1.5 V and 2.5 V. However, both the separators (SIL BH and SIL SH) in SIBs performed well compared to other separators, as silicone has excellent thermal and electrical insulating properties and the holes on the surface of silicone bear a high loading of gel-polymer electrolyte. In addition, silicone rubber has a high pore size (5.27 ± 1.44 to 218.03 ± 17.95 μm) [59, 60] that enhances the electrolyte-uptake property and allows the movement of Na-ions from cathode to anode and anode to cathode during charge and discharge processes.

The cyclic performances of CQDs@SnO_2 and CQDs@$NaVO_3$ in different separators were also evaluated at 1 and

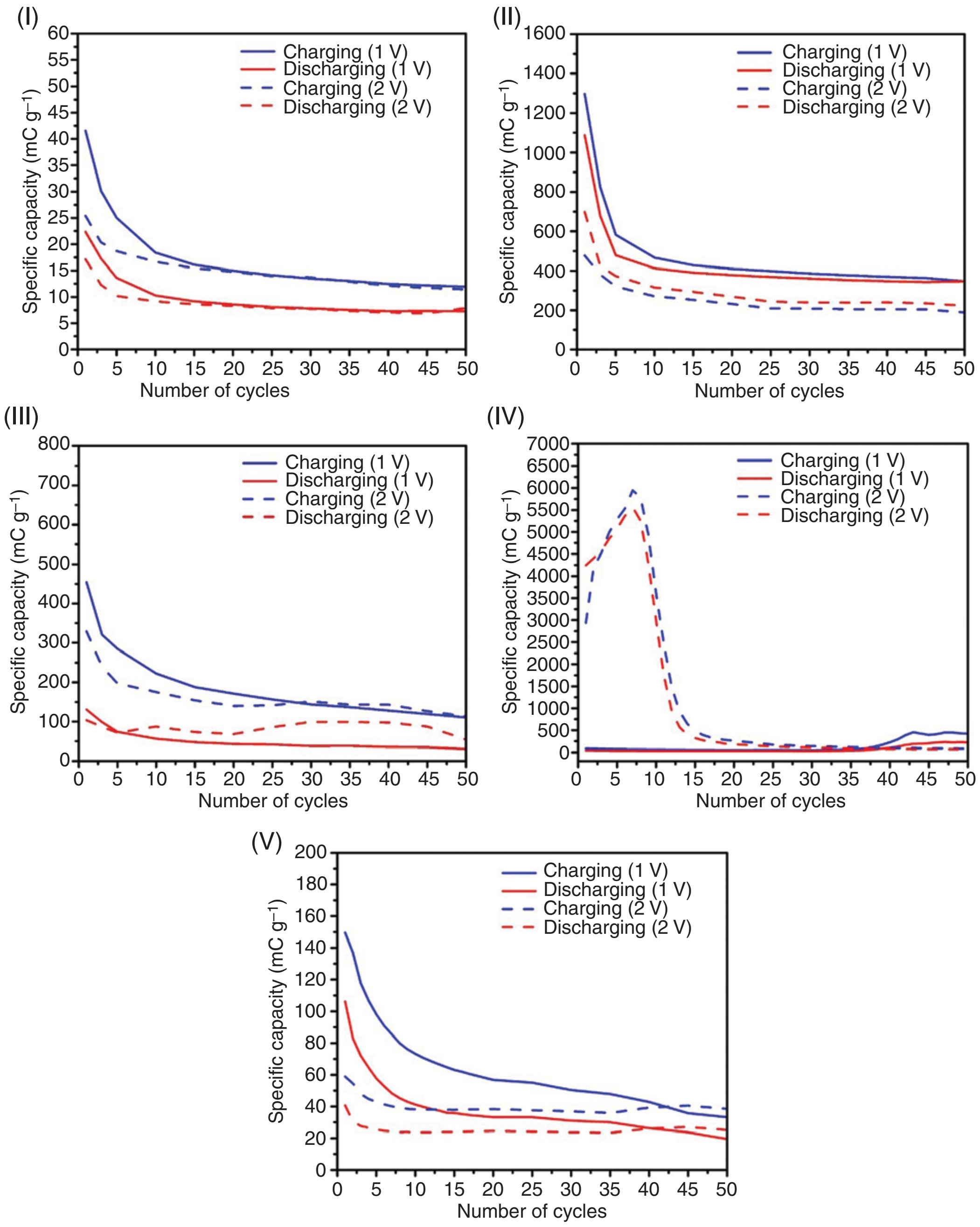

Fig. 10: Cycling performance of SIBs using various separators at 1 and 2 V (I) ITO/PTE, (II) RP, (III) SIL BH, (IV) SIL SH and (V) CP

2 V and are shown in Fig. 10I–V. The raw data from Autolab are shown in Fig. S3I–V in the online Supplementary Data. RP had a specific charge capacity of 1298 mC g^{-1} in the first cycle at 1 V and subsequently the charge capacity reduced to 466, 398 and 365 in the 10th, 25th and 50th cycles. It delivered good specific discharge capacities at 1087, 412, 368 and 347 mC g^{-1} in the 1st, 10th, 25th and 50th cycles at 1 V. In the ITO/PTE separator, there is poor performance in charge and discharge behaviour, as ITO has a low porosity that may affect the sodiation/desodiation process during charge and discharge processes. SIL BH delivered a specific charge and discharge capacity of 455 and 131 mC g^{-1} in the first cycle at 1 V (Fig. 10III), which are higher than SIL SH (88 and 45 mC g^{-1}) (Fig. 4). In the 50th cycle, SIL SH delivered higher specific charge and discharge capacities (420 and 225 mC g^{-1}) than SIL BH (110 and 30 mC g^{-1}). CP has a good charge and discharge cyclability compared to that of ITO/PTE at 1 and 2 V, as ITO/PTE has low surface resistivity (60 Ω sq^{-1}). At 2 V, RP delivered a lower specific charge capacity (477 mC g^{-1}) than at 1 V (1298 mC g^{-1}) in the first cycle, whereas it delivered a lower specific charge capacity (222 mC g^{-1}) than 1 V (347 mC g^{-1}) in the 50th cycle (Fig. 10II). The charge- and discharge-specific capacities are low at a high voltage (2 V) in RP, SIL BH and CP. However, SIL SH delivered high initial specific charge capacities in the 1st and 10th cycles (2938 and 3621 mC

g^{-1}) at 2 V whereas, in the 25th and 50th cycles, it shows lower (171 and 83 mC g^{-1}) specific charge capacity than RP and SIL BH. The delivery of high capacity in the first cycle that is higher than the theoretical capacity of the anode (CQDs@SnO_2) is due to the formation of an SEI layer [21]. The specific discharge capacity of RP is high in the 1st and 10th cycles and reduces gradually over 1 and 2 V. The specific discharge capacities of RP are 347 and 224 mC g^{-1} in the 50th cycle at both 1 and 2 V. RP has a steady charge and discharge cyclability in all the cycles and is not known to alter the physical and chemical properties of the active materials present on the surface of the electrode. The loss of Na-ions is prevented with improvement in the ability of the electrodes to intercalate and deintercalate the Na-ions during the charging and discharging processes [61].

SIL SH delivered a specific discharge capacity of 223 mC g^{-1} in the 50th cycle at 1 V, which is lower than that of RP (347 mC g^{-1}). SIL SH has a high initial specific discharge capacity of 4246 mC g^{-1} at 2 V compared to other separators, whereas it delivered a low capacity (45 mC g^{-1}) at 1 V. In SIL SH, the capacity decay was rated as 45 mC g^{-1} from the initial cycle to 30 mC g^{-1} in the 21st cycle at 1 V (Fig. 10IV), which may be caused by the large size of the active materials with carbon black formed by the aggregation of the particles. It may be hard for the sodium ions to deintercalate into active materials. The specific charge and discharge capacities suddenly increase from the 31st to the 50th cycle due to the formation of a stable SEI film consequent to the activation of the carbon material by the repeated intercalation and deintercalation of Na-ions [56, 62]. The increase in the discharge capacities of SIL SH after the 35th cycle reveals the formation of a gel-like reversible polymer film on the surface of the CQDs [56]. The maximum specific charge capacities of SIL SH were obtained in 48th and 47th cycles (233 and 228 mC g^{-1}) at 1 V. At 2 V, the trend was reversed. SIL SH delivered high specific discharge capacities up to the 13th cycle. From the 15th to the 50th cycle, it showed low discharge capacities. SIL SH had poor specific charge and discharge capacities after the 20th cycle at 2 V (Fig. 10IV). Different discharge rates observed at 2V in the SIL BH separator affects the capacity of the battery (Fig. 10III). A rapid drop in capacity during the first few cycles (up to the 12th cycle) of the battery (SIL SH at 2 V) at high charge and discharge rates (Fig. 10IV) reveals that the internal resistance of the battery is high. The silicone-based separators, examined at two different voltages (1 and 2 V), are known to suffer capacity losses apparently due to the limitation in the ability of the electrode material in the sodiation or desodiation process. The surface film on the electrode may bring about a change in the voltage, gel-polymer electrolyte, agglomeration between the particles in the electrode and the physical dimension of the separators affecting the electrode's ability in the sodiation and desodiation processes [61]. The specific power and energy as the derivatives of time, current and voltage of all fabricated batteries were calculated in the 1st, 10th, 25th and 50th cycles at two different voltages (1 and 2 V) (Table 2).

Table 2: Specific power and energy of all fabricated batteries in various cyclic abilities at 1 and 2 V

Various separators in SIBs	Charging at 1 V								Discharging at 1 V							
	1st cycle		10th cycle		25th cycle		50th cycle		1st cycle		10th cycle		25th cycle		50th cycle	
	Specific power (mW g^{-1})	Specific energy (Wh g^{-1})	Specific power (mW g^{-1})	Specific energy (Wh g^{-1})	Specific power (mW g^{-1})	Specific energy (Wh g^{-1})	Specific power (mW g^{-1})	Specific energy (Wh g^{-1})	Specific power (mW g^{-1})	Specific energy (Wh g^{-1})	Specific power (mW g^{-1})	Specific energy (Wh g^{-1})	Specific power (mW g^{-1})	Specific energy (Wh g^{-1})	Specific power (mW g^{-1})	Specific energy (Wh g^{-1})
ITO/PTE	42.67	12.45	18.55	5.51	14.28	4.23	12.12	3.58	23.33	6.69	10.43	3.08	14.28	4.23	7.42	2.18
RP	1307.83	389.09	467.51	139.75	399.68	119.41	366.42	109.43	1098.85	325.97	413.63	123.59	369.76	110.43	348.43	104.04
SIL BH	461.84	136.24	223.87	66.65	157.97	46.89	112.02	33.11	135.81	39.07	57.94	16.90	43.27	12.50	31.95	9.10
SIL SH	92.00	26.33	63.56	18.58	54.59	15.89	421.40	125.90	46.31	13.41	33.89	9.68	31.59	9.00	226.13	67.32
CP	153.08	44.83	74.87	21.97	56.62	16.50	33.18	9.94	107.68	31.82	42.71	12.33	34.81	9.96	21.06	5.84
	Charging at 2 V								**Discharging at 2 V**							
ITO/PTE	53.94	15.22	33.70	10.01	28.24	8.37	23.19	6.85	37.36	10.27	18.64	5.49	16.09	4.73	14.07	4.12
RP	1005.01	285.80	544.85	162.47	421.53	125.48	381.04	113.34	1399.39	418.77	633.92	189.18	490.17	146.07	447.46	133.26
SIL BH	691.98	197.23	353.62	105.07	286.18	84.85	230.12	68.04	216.97	62.00	177.88	52.37	175.39	51.61	111.13	32.43
SIL SH	5980.47	1761.87	7368.77	2171.48	345.65	102.65	169.94	49.99	8600.71	2546.99	6126.51	1800.92	276.91	77.83	144.80	42.45
CP	123.47	35.31	79.56	22.90	78.37	22.55	80.10	23.06	84.34	24.34	50.52	14.19	51.44	14.47	53.61	15.12

EIS was performed to study the resistance of charge transfer (R_{ct}) and Na-ion diffusion. The ion-diffusion behaviour between the electrodes and the gel-polymer electrolyte was examined from the slope at the low-frequency region of the Nyquist plot. In the high-frequency region of the Nyquist plot, the R_{ct} is acquired from the diameter of the semicircle of the charge-transfer resistance occurring at the interface of the electrode and the electrolyte [63, 64]. ITO/PTE shows a larger semicircle with the R_{ct} value (~280 kΩ) than the other separators (Fig. S4 in the online Supplementary Data). The large semicircle indicates that PVA/P3HT has high interfacial resistance in ITO/PTE with poor charge propagation [65]. The diameter of the above semicircle is small when compared to those of RP, SIL BH, SIL SH and CP. In this study, PVA with a P3HT gel-polymer electrolyte was used. PVA has a low electrical conductivity (1.63×10^{-12} S cm^{-1} at RT) whereas P3HT has high electrical conductivity (12.7 S cm^{-1}). PVA and P3HT were used at a weight ratio of 1:0.05. P3HT is used as a solution in chloroform. It is reported that the P3HT-g-PVA prepared in hexane has higher electrical conductivity (6.9×10^{-7} S cm^{-1}) than P3HT-g-PVA prepared in chloroform (3.3×10^{-8} S cm^{-1}) or in acetonitrile (2.9×10^{-8} S cm^{-1}) [66]. High interfacial resistance is reported to occur in the presence of a large amount of PVA with P3HT. An equivalent circuit for the EIS data is shown in the inset of Fig. S4 in the online Supplementary Data. R_i, C, R_{ct} and W are the internal resistance, capacitance, charge-transfer resistance and Warburg resistance (mass-transfer resistance) of the SEI layers. R_i represents the bulk resistance of the cell, which includes the resistance due to the electrodes, separator and electrolyte [67]. The straight line at low frequencies is the Warburg impedance, which is directly associated with the diffusion of the Na-ion at the electrode–electrolyte interface [68]. SIL SH and SIL BH have low interfacial resistance compared to the other separators. In addition, they have high charge-transfer resistances compared to the other separators of RP, CP (moderate) and ITO/PTE (low). They have a low range of interfacial resistance (~400 Ω), as the silicone rubber has a high electrical insulating property (1–100 TΩ). CP starts from an interfacial resistance of ~560 Ω, which is slightly higher than that of SIL BH and SIL SH. CP, a universal material, is known to function as a good insulator. On account of its capacitance, ITO/PTE shows a higher performance than CP, SIL BH and SIL SH. CP has higher initial resistance than ITO/PTE, SIL BH and SIL SH. ITO/PTE expresses higher mass-transfer resistance than RP, SIL BH and SIL SH than that of CP due to the large pore size with more distribution on the surface area. This study reveals that the high ratio (>1:0.05) between PVA and P3HT and an effective insulating material (silicone) as the separator can effectively enhance the performance of SIBs.

3 Conclusion

CQDs were prepared using the alkaline-peroxide-assisted hydrothermal carbonization method from the dead leaves of the tree *S. saman* with a quantum yield of 21.03% at an excitation wavelength of 360 nm. These CQDs were decorated with SnO_2 and $NaVO_3$, and used as anode and cathode materials in flexible Na-ion batteries. CQD showed sp^2 and sp^3 stretching vibration modes of hybridized carbon atoms at the surface. CQDs, CQDs@SnO_2 and CQDs@$NaVO_3$ showed excitation-dependent wavelengths. The average crystalline sizes of the uncalcined CQDs, calcined CQDs, CQDs@SnO_2 and CQDs@$NaVO_3$ were 12.8, 11.5, 11.9 and 14.4 nm. Calcined CQDs exhibited a hexagonal structure with an interlayer spacing of 0.37 nm as known from XRD and TEM studies and occurred as nanorods with a porous structure. CQDs@SnO_2 was of crystalline nature with several lattice planes whereas CQDs@$NaVO_3$ was of nanorods with tiny porous crystals on the surface. The performance of five separators (ITO/PTE, RP, SIL BH, SIL SH and CP) in flexible Na-ion batteries was evaluated. CV studies showed that the silicone-based separator SIL SH showed higher specific capacitance (881 F g^{-1}) than SIL BH (116 F g^{-1}). The specific discharge capacities of RP during the 1st, 10th, 25th and 50th cycles at 1 V were 1087, 412, 368 and 347 mC g^{-1}. The charge- and discharge-specific capacities were observed to reduce at 2 V in RP, SIL BH and CP. SIL SH displayed a high initial specific discharge capacity in the 1st and 10th cycles (4246 and 3003 mC g^{-1}) at 2 V whereas, in the 25th and 50th cycles, there were lower specific discharge capacities (130 and 71 mC g^{-1}) than those of CP and SIL BH. SIL SH and SIL BH have higher specific capacitance than the other separators whereas RP has better cyclic stability than the other separators. RP is edible and therefore it is not encouraged to be used as a separator due to the expected conflict. In the context of using PVA/P3HT gel as a polymer electrolyte, there is a need to optimize the concentration of P3HT for use in SIBs. Once the gel-polymer electrolyte is optimized, silicone-sheet separators of different thicknesses and dimensions are to be studied so as to enhance the performance level of batteries. Besides, different binary metal oxides having nanostructured porous carbon and polyanion sodium hosts are to be tried as anodes and cathodes to improve the performance of flexible SIBs.

Supplementary data

Supplementary data is available at *Clean Energy* online.

Acknowledgements

One of the authors (B.T.) expresses his gratitude to King Mongkut's University of Technology Thonburi (KMUTT) for the Postdoctoral fellowship awarded to him and the Research Network NANOTEC (RNN) program (Grant No: P1851883) of the National Nanotechnology Center (NANOTEC), NSTDA, Ministry of Science and Technology, Thailand that made this work possible. His thanks are due to the Fuel Cells and Hydrogen Research and Engineering Center, KMUTT for assisting in the electrochemical impedance spectra study.

Conflict of Interest

None declared.

References

[1] Feng Y, Chen S, Wang J, *et al*. Carbon foam with microporous structure for high performance symmetric potassium dual-ion capacitor. *Journal of Energy Chemistry,* 2020, 43:129–138.

[2] Ellis BL, Nazar LF. Sodium and sodium-ion energy storage batteries. *Current Opinion in Solid State and Materials Science,* 2012, 16:168–177.

[3] Górka J, Vix-Guteri C, Ghimbeu CM. Recent progress in design of biomass-derived hard carbons for sodium ion batteries. *Journal on Carbon Research,* 2016, 2:1–17.

[4] Guo L, An Y, Fei H, *et al*. Self-templated biomass-derived nitrogen-doped porous carbons as high-performance anodes for sodium ion batteries. *Materials and Technology,* 2017, 32:592–597.

[5] Zhang Q, Cheng X, Wang C, *et al*. Sulfur-assisted large-scale synthesis of graphene microspheres for superior potassium-ion batteries. *Energy & Environmental Science,* 2021,11:965–974.

[6] Liu Y, Liu D, Zhang Q, *et al*. Lithium iron phosphate/carbon nanocomposite film cathodes for high energy lithium ion batteries. *Electrochimica Acta,* 2011, 56:2559–2565.

[7] Kim K, Lim DG, Han CW, *et al*. Tailored carbon anodes derived from biomass for sodium-ion storage. *ACS Sustainable Chemistry & Engineering,* 2017, 5:8720–8728.

[8] Palomares V, Serras P, Villaluenga I, *et al*. Na-ion batteries, recent advances and present challenges to become low cost energy storage systems. *Energy & Environmental Science,* 2012, 5:5884–5901.

[9] Hou, H, Qiu X, Wei W, *et al*. Carbon anode materials for advanced sodium-ion batteries. *Advanced Energy Materials,* 2017,7:1–30.

[10] Hou H, Banks CE, Jing M, *et al*. Carbon quantum dots and their derivative 3D porous carbon frameworks for sodium-ion batteries with ultralong cycle life. *Advanced Materials,* 2015,27:7861–7866.

[11] Hu Z, Liu Z, Zhao J, *et al*. Rose-petals-derived hemispherical micropapillae carbon with cuticular folds for super potassium storage. *Electrochimica Acta,* 2021, 368:1–7.

[12] Liu ML, Chen BB, Li CM, *et al*. Carbon dots: synthesis, formation mechanism, fluorescence origin and sensing applications. *Green Chemistry,* 2019, 21:449–471.

[13] Thangaraj B, Solomon PR, Ranganathan S. Synthesis of carbon quantum dots with special reference to biomass as a source—a review. *Current Pharmaceutical Design,* 2019,25:1455–1476.

[14] Thangaraj B, Solomon PR. Biodiesel production by the electrocatalytic process: a review. *Clean Energy,* 2021, 5: 19–31.

[15] Prasannan A, Imae T. Carbon dots: synthesis, formation mechanism, fluorescence origin and sensing applications. *Industrial & Engineering Chemistry Research,* 2013, 52:15673–15678.

[16] Zhou J, Sheng Z, Han HY, *et al*. Facile synthesis of fluorescent carbon dots using watermelon peel as a carbon source. *Materials Letters,* 2012, 66:222–224.

[17] Mewada A, Pandey S, Shinde S, *et al*. Green synthesis of biocompatible carbon dots using aqueous extract of *Trapa bispinosa* peel. *Materials Science and Engineering: C,* 2013,33:2914–2917.

[18] Pourreza N, Ghomi M. Green synthesized carbon quantum dots from *Prosopis juliflora* leaves as a dual off-on fluorescence probe for sensing mercury (II) and chemet drug. *Materials Science and Engineering: C,* 2019,98:887–896.

[19] Jiang Q, Zhang Z, Yin S, *et al*. Biomass carbon micro/nano-structures derived from ramie fibers and corncobs as anode materials for lithium-ion and sodium-ion batteries. *Applied Surface Science,* 2016, 379:73–82.

[20] Fang Y, Yu XY, Lou XW. Nanostructured electrode materials for advanced sodium-ion batteries. *Matter,* 2019, 1:90–114.

[21] Liu Q, Dou Y, Ruan B, *et al*. Carbon-coated hierarchical SnO_2 hollow spheres for lithium ion batteries. *Chemistry—A European Journal,* 2016, 22:5853–5857.

[22] Gao M, Zhou P, Wang P, *et al*. FeO/C anode materials of high capacity and cycle stability for lithium-ion batteries synthesized by carbothermal reduction. *Journal of Alloys and Compounds,* 2013, 565:97–103.

[23] Rai AK, Anh LT, Gim J, *et al*. One-step synthesis of CoO anode material for rechargeable lithium-ion batteries. *Ceramics International,* 2013, 39:9325–9330.

[24] Jing M, Wang J, Hou H, *et al*. Carbon quantum dot coated Mn_3O_4 with enhanced performances for lithium-ion batteries. *Journal of Materials Chemistry A,* 2015, 3:16824–16830.

[25] Wang Q, Xu J, Zhang W, *et al*. Research progress on vanadium-based cathode materials for sodium ion batteries. *Journal of Materials Chemistry A,* 2018, 6:8815–8838.

[26] Hu F, Jiang W, Dong Y, *et al*. Synthesis and electrochemical performance of NaV_6O_{15} microflowers for lithium and sodium ion batteries. *RSC Advances,* 2017, 7:29481–29488.

[27] Song X, Li J, Li Z, *et al*. Superior sodium storage of carbon-coated NaV_6O_{15} nanotube cathode: pseudocapacitance versus intercalation. *ACS Applied Materials & Interfaces,* 2019,11:10631–10641.

[28] Cui Y, Chai J, Du H, *et al*. Facile and reliable in situ polymerization of poly(ethyl cyanoacrylate)-based polymer electrolytes toward flexible lithium batteries. *ACS Applied Materials & Interfaces,* 2017,9:8737–8741.

[29] Yang M, Hou J. Membranes in lithium ion batteries. *Membranes,* 2012,2:367–383.

[30] Tan L, Deng Y, Cao Q, *et al*. Gel electrolytes based on polyacrylonitrile/thermoplastic polyurethane/polystyrene for lithium-ion batteries. *Ionics,* 2019, 25:3673–3682.

[31] Zhan J, Peng R, Wei S, *et al*. Ethanol-precipitation-assisted highly efficient synthesis of nitrogen-doped carbon quantum dots from chitosan. *ACS Omega,* 2019,4:22574–22580.

[32] Sun K, Ran F, Zhao G, *et al*. High energy density of quasi-solid-state supercapacitor based on redox-mediated gel polymer electrolyte. *RSC Advances,* 2016, 6:55225–55232.

[33] Delgado DC, Hera R, Cairo J, *et al*. *Samanea saman*, a multi-purpose tree with potentialities as alternative feed for animals of productive interest. *Cuban Journal of Agricultural Science,* 2014, 48:205–212.

[34] Libra JA, Ro KS, Kammann C, *et al*. Hydrothermal carbonization of biomass residuals: a comparative review of the chemistry, processes and applications of wet and dry pyrolysis. *Biofuels,* 2011, 2:89–124.

[35] Gómez J, Corsi G, Pino-Cortés E, *et al*. Modeling and simulation of a continuous biomass hydrothermal carbonization process. *Chemical Engineering Communications,* 2020, 207:751–768.

[36] Reza MT, Wirth B, Lüder U, *et al*. Behavior of selected hydrolyzed and dehydrated products during hydrothermal carbonization of biomass. *Bioresource Technology,* 2014,169:352–361.

[37] Jing S, Zhao Y, Sun RC, *et al*. Facile and high-yield synthesis of carbon quantum dots from biomass-derived carbons at mild condition. *ACS Sustainable Chemistry & Engineering,* 2019, 7:7883–7843.

[38] Wu CY, Tu KJ, Deng JP, *et al*. Markedly enhanced surface hydroxyl groups of TiO_2 nanoparticles with superior water-dispersibility for photocatalysis. *Materials,* 2017, 10:1–15.

[39] Yadav PK, Singh VK, Chandra S, *et al*. Green synthesis of fluorescent carbon quantum dots from *Azadirachta indica* leaves and their peroxidase-mimetic activity for the detection of H_2O_2 and ascorbic acid in common fresh fruits. *ACS Biomaterials Science & Engineering,* 2019,5:623–632.

[40] Zhu L, Yin Y, Wang CF, *et al*. Plant leaf-derived fluorescent carbon dots for sensing, patterning and coding. *Journal of Materials Chemistry C,* 2013, 32:4925–4932.

[41] Raveendran V, Suresh Babu AR, Renuka NK. Mint leaf derived carbon dots for dual analyte detection of Fe(iii) and ascorbic acid. *RSC Advances,* 2019, 9:12070–12077.

[42] Liu Y, Zhao Y, Zhang Y. One-step green synthesized fluorescent carbon nanodots from bamboo leaves for copper(II) ion detection. *Sensors and Actuators B,* 2014, 196:647–652.

[43] Zhao X, Liao S, Wang L, *et al*. Facile green and one-pot synthesis of *purple perilla* derived carbon quantum dot as a fluorescent sensor for silver ion. *Talanta,* 2019,201:1–8.

[44] Jhonsi MA, Thulasi S. A novel fluorescent carbon dots derived from tamarind. *Chemical Physics Letters,* 2016, 661:179–184.

[45] Sahu S, Behera B, Maiti TK, *et al*. Simple one-step synthesis of highly luminescent carbon dots from orange juice: application as excellent bio-imaging agents. *Chemical Communications,* 2012,48:8835–8837.

[46] Park SY, Lee HU, Park ES, *et al*. Photoluminescent green carbon nanodots from food-waste-derived sources: large-scale synthesis, properties, and biomedical applications. *ACS Applied Materials & Interfaces,* 2014,6:3365–3370.

[47] Zhu C, Zhai J, Dong S. Bifunctional fluorescent carbon nanodots: green synthesis via soy milk and application as metal-free electrocatalysts for oxygen reduction. *Chemical Communications,* 2012;48,9367–9369.

[48] Deng L, Wang X, Kuang Y, *et al*. Development of hydrophilicity gradient ultracentrifugation method for photoluminescence investigation of separated non-sedimental carbon dots. *Nano Research,* 2015, 8:2810–2821.

[49] Xie F, Xu Z, Guo Z, *et al*. Hard carbons for sodium-ion batteries and beyond. *Progress in Energy,* 2020, 2:1–30.

[50] Liu S, Liu R, Xing X, *et al*. Highly photoluminescent nitrogen-rich carbon dots from melamine and citric acid for the selective detection of iron(iii) ion. *RSC Advances,* 2016, 6:31884–31888.

[51] Wang K, Xu Y, Li Y, *et al*. Sodium storage in hard carbon with curved graphene platelets as the basic structural units. *Journal of Materials Chemistry A,* 2019, 7:3327–3335.

[52] Hou H, Shao L, Zhang Y, *et al*. Large-area carbon nanosheets doped with phosphorous: a high-performance anode material for sodium-ion batteries. *Advanced Science,* 2016, 4:1–11.

[53] Kim J, Seo DH, Kim H, *et al*. Unexpected discovery of low-cost maricite $NaFePO_4$ as a high-performance electrode for Na-ion batteries. *Energy & Environmental Science,* 2015, 8:540–545.

[54] Xu K, Li Y, Xiong J, *et al*. Activated amorphous carbon with high-porosity derived from camellia pollen grains as anode materials for lithium/sodium ion batteries. *Frontiers in Chemistry,* 2018,6:366.

[55] Kim SW, Seo DH, Ma X, *et al*. Electrode materials for rechargeable sodium-ion batteries: potential alternatives to current lithium-ion batteries. *Advanced Energy Materials,* 2012, 2:710–721.

[56] Gao X, An Y, Zhang W, *et al*. Self-supporting soft carbon fibers as binder-free and flexible anodes for high-performance sodium-ion batteries. *Materials and Technology,* 2018, 33:810–814.

[57] Aurbach D, Markovsky B, Salitra G, *et al*. Review on electrode–electrolyte solution interactions, related to cathode materials for Li-ion batteries. *Journal of Power Sources,* 2007, 165:491–499.

[58] Wang H, Pilon L. Physical interpretation of cyclic voltammetry for measuring electric double layer capacitances. *Electrochimica Acta,* 2012, 64:130–139.

[59] Xu R, Bai Y, Zhao J, *et al*. Silicone rubber membrane with specific pore size enhances wound regeneration. *Journal of Tissue Engineering and Regenerative Medicine,* 2017, 12:e905–e917.

[60] Ning G, Haran B, Popov BN. Capacity fade study of lithium-ion batteries cycles at high discharge rates. *Journal of Power Sources,* 2003, 117:160–169.

[61] Xie F, Zhang L, Su D, *et al*. $Na_2Ti_3O_7$@N-doped carbon hollow spheres for sodium-ion batteries with excellent rate performance. *Advanced Materials,* 2017, 29:1–6.

[62] Liu Y, Lin D, Yuen P, *et al*. An artificial solid electrolyte interphase with high li-ion conductivity, mechanical strength, and flexibility for stable lithium metal anodes. *Advanced Materials,* 2016, 29:1–8.

[63] Lim J, Ryu SY, Kim J, *et al*. A study of TiO_2/carbon black composition as counter electrode materials for dye-sensitized solar cells. *Nanoscale Research Letters,* 2013, 8:1–5.

[64] Si P, Ding S, (David) Lou XW, *et al*. An electrochemically formed three-dimensional structure of polypyrrole/graphene nanoplatelets for high-performance supercapacitors. *RSC Advances,* 2011, 1:1271–1278.

[65] Ding H, Zhou J, Rao AM, *et al*. Cell-like-carbon-micro-spheres for robust potassium anode. *National Science Review,* 2020, nwaa276:1–9.

[66] Hai TAP, Sugimoto R. Synthesis and characterization of poly(3-hexylthiophene)-grafted polyvinyl alcohol. *Synthetic Metals,* 2018, 240:37–43.

[67] Zhang SS, Xu K, Jow TR. EIS study on the formation of solid electrolyte interface in Li-ion battery. *Electrochimica Acta,* 2006, 51:1636–1640.

[68] Chandra M, Khan TS, Shukla R, *et al*. Diffusion coefficient and electrochemical performance of $NaVO_3$ anode in Li/Na batteries. *Electrochimica Acta,* 2020, 331:135293.